Fructose-stimulated *de novo* lipogenesis depends on inflammation

Jelena Todoric[1,2], Giuseppe Di Caro[1], Saskia Reibe[3], Darren C. Henstridge[4], Courtney R. Green[5], Alison Vrbanac[6], Fatih Ceteci[7,8,9], Claire Conche[7,8,9], Shabnam Shalapour[1], Koji Taniguchi[1,10], Reginald McNulty[1], Peter Meikle[4], Jeramie D Watrous[11], Rafael Moranchel[11], Mahan Najhawan[11], Mohit Jain[11], Xiao Liu[11], Tatiana Kisseleva[11], Maria T. Diaz-Meco[12], Jorge Moscat[12], Rob Knight[13], Florian R. Greten[7,8,9], Lester F. Lau[14], Christian M. Metallo[5], Mark A. Febbraio[3,15], and Michael Karin[1, *]

[1]Laboratory of Gene Regulation and Signal Transduction, Department of Pharmacology, School of Medicine, University of California San Diego, 9500 Gilman Drive, La Jolla, CA 92093, USA

[2]Department of Laboratory Medicine, Medical University of Vienna, Vienna, 1090, Austria

[3]Garvan Institute of Medical Research, 384 Victoria St, Darlinghurst NSW 2010, Sydney, Australia

[4]Baker Heart and Diabetes Institute, 75 Commercial Rd, Melbourne, VIC, 3004, Australia

[5] Department of Bioengineering, University of California, San Diego, La Jolla, CA 92093, USA.

[6]Biomedical Sciences Graduate Program, University of California San Diego, La Jolla, CA 92093, USA

[7]Institute for Tumor Biology and Experimental Therapy, Georg-Speyer-Haus, 60596 Frankfurt/Main, Germany

[8]Frankfurt Cancer Institute, Goethe University Frankfurt, 60596 Frankfurt/Main, Germany

[9]German Cancer Consortium (DKTK) and German Cancer Research Center (DKFZ), 69120 Heidelberg, Germany

[10]Department of Microbiology and Immunology, Keio University School of Medicine, Tokyo 160-8582, Japan

[11]Departments of Medicine and Pharmacology, University of California San Diego, La Jolla, CA 92093, USA

[12]Cancer Metabolism and Signaling Networks Program, Sanford Burnham Prebys Medical Discovery Institute, La Jolla, CA 92037, USA

[13]Department of Pediatrics, Department of Computer Science and Engineering, Department of Bioengineering, and The Center for Microbiome Innovation, University of California, San Diego, La Jolla, CA 92093, USA

[14]Department of Biochemistry and Molecular Genetics, University of Illinois at Chicago College of Medicine, Chicago, IL 60607, USA

15Drug Discovery Biology, Monash Institute of Pharmaceutical Sciences, Monash University, Parkville, VIC, 3052, Australia

*Correspondence to: karinoffice@ucsd.edu

Abstract

Benign hepatosteatosis, affected by lipid uptake, *de novo* lipogenesis and fatty acid (FA) oxidation, progresses to non-alcoholic steatohepatitis (NASH) on stress and inflammation. A key macronutrient proposed to increase hepatosteatosis and NASH risk is fructose, whose excessive intake causes intestinal barrier deterioration and endotoxemia. However, how fructose triggers these alterations and their role in hepatosteatosis and NASH pathogenesis remain unknown. By preventing fructose and endoplasmic reticulum stress-dependent barrier deterioration and subsequent endotoxemia using a chemical chaperon, activation of mucosal-regenerative gp130 signaling, administration of the YAP-induced matricellular protein CCN1 or expression of anti-microbial Reg3β peptide, we show that microbiota-derived Toll-like receptor (TLR) agonists promote hepatosteatosis without affecting fructose-1 phosphate (F1P) and cytosolic acetyl-CoA. TLR engagement triggers TNF production by liver macrophages to induce lipogenic enzymes that convert F1P and acetyl-CoA to FA in mouse and human hepatocytes.

Keywords: NASH, NAFLD, *de novo* lipogenesis, fructose, gut-liver axis, TNF

Non-alcoholic steatohepatitis (NASH), a severe manifestation of non-alcoholic fatty liver disease (NAFLD) which affects 30% of adult Americans[1], is a leading cause of liver failure, cirrhosis and cancer[2]. NAFLD starts as simple steatosis with little liver damage or fibrosis, whose progression to NASH depends on multiple parallel hits acting in concert with hepatosteatosis. The latter can be due to increased lipid import, enhanced *de novo* lipogenesis (DNL), or impaired β oxidation[3]. Proposed hits include gut-derived inflammatory signals and endoplasmic reticulum (ER) stress[3–7]. Having established a role for ER stress and TNF signaling in NASH pathogenesis[8,9], we sought to unravel the role of gut-derived inflammatory signals linked to fructose-induced barrier deterioration. Fructose, whose US consumption had increased several thousand-fold, is a key macronutrient that may contribute to NASH development[10]. Fructose causes barrier deterioration through a heretofore unknown mechanism entailing downregulation of tight junction proteins (TJP) in animal subjects and pediatric patients[11–13]. Fructose also triggers dysbiosis[14] and its metabolism by gut bacteria generates short chain fatty acids (SCFA)[15], proposed to improve barrier function[16,17]. Unlike glucose, which is generated by hydrolysis of starch and is metabolically mobilized by the highly regulated enzyme glucokinase, fructose is phosphorylated by the constitutively active enzyme fructokinase (also known as ketohexokinase/KHK)[18], that is particularly active in hepatocytes in which it stimulates DNL and hepatic fat deposition[10,19]. DNL depends on two key enzymes, acetyl CoA carboxylase (ACC) and fatty acid synthase (FAS), whose expression is induced by fructose[20]. Here we show that gut barrier deterioration and subsequent endotoxemia result in hepatic induction of ACC1 and FAS and other SREBP1-activated lipogenic genes to upregulate DNL without an effect on KHK-dependent fructose-1 phosphate (F1P) and cytosolic acetyl-CoA accumulation. Fructose-elicited endotoxemia activates Toll-like receptor (TLR) signaling in liver macrophages, whose blockade via myeloid-specific MyD88 ablation prevents TNF, ACC1 and FAS induction and attenuates hepatosteatosis. Conversely, addition of TNF to

cultured human hepatocytes enhances fructose conversion to lipids. Correspondingly, genetic and pharmacological manipulations that prevent ER stress-dependent fructose-induced barrier deterioration and endotoxemia block fructose-stimulated DNL, hepatosteatosis and the onset of steatohepatitis and cancer.

Results

Fructose stimulates DNL and triggers hepatosteatosis, steatohepatitis and HCC

Transgenic (Tg) *MUP-uPA* mice expressing high amounts of urokinase plasminogen activator (uPA) from a liver-specific promoter were used to establish a causal role for hepatocyte ER stress in NASH pathogenesis[8]. Although *MUP-uPA* mice older than 8 weeks kept on normal chow diet (NCD) do not display obvious hepatic abnormalities, when placed on energy-rich high fat diet (HFD) they manifest classical NASH signs within 3-4 months and progress to hepatocellular carcinoma (HCC) by 9-10 months. Prevention of hepatocyte ER stress blocks NASH development[8] by inhibiting IRE-1 dependent translation and subsequent activation of caspase-2[9]. Induction of C*aspase-2* mRNA requires TNF signaling, whose blockade also blocks NASH development[8,9]. The mechanism by which HFD induces TNF secretion by liver macrophages is unknown. We used the *MUP-uPA* model and parental BL6 mice to investigate whether fructose-induced DNL can elicit NASH and subsequent HCC development. Both *MUP-uPA* and BL6 mice were given isocaloric low-fat and carbohydrate-rich diets containing either fructose or cornstarch (CS), a polymer that is readily hydrolyzed to glucose. Whereas high fructose diet (HFrD) contains 10% CS and 60% fructose, the CS diet (CSD) derives 70% of its calories from CS. Although diet consumption was similar, HFrD, but not CSD, induced hepatosteatosis and increased liver triglycerides (TG) in both strains (Fig. 1a, b and Extended Data Fig. 1a-c). Steatohepatitis, ballooning degeneration and liver fibrosis were apparent in 6-month-old HFrD-fed *MUP-uPA* mice, but BL6 mice only showed benign steatosis. HFrD feeding did not cause adiposity and white adipose tissue (WAT) was somewhat smaller in HFrD-fed animals (Extended

Data Fig. 1d, e). HFrD feeding induced colon shortening, a sign of intestinal inflammation (Extended Data Fig. 1f) and caused more insulin resistance than CSD, as shown by glucose tolerance tests (GTT), while mildly decreasing energy expenditure in 6-month-old mice kept in metabolic cages, which did not differ in weight gain (Extended Data Fig. 1g-j). Consistent with insulin-resistance, non-fasting insulin was higher in HFrD-fed mice (Extended Data Fig. 1k). After 12 months, HFrD-fed *MUP-uPA* mice exhibited 3-fold more HCC nodules that were larger than those in CSD-fed mice, resulting in 10-fold higher tumor burden (Fig. 1c, d). HFrD also enhanced diethyl nitrosamine (DEN)-induced HCC in BL6 mice, which do not develop cancer without it (Fig. 1e). Most tumors in HFrD-fed mice were poorly differentiated, steatotic HCCs (Extended Data Fig. 1l).

The cytosolic pool of acetyl-CoA, needed to initiate DNL, was two-fold higher in HFrD- than CSD-fed *MUP-uPA* mice (Extended Data Fig. 2a). Prolonged HFrD consumption markedly upregulated hepatic mRNAs for SREBP1c (*Srebf1*), carbohydrate-responsive element-binding protein (ChREBP/*Mlxipl*) and the SREBP1-regulated enzymes ACC1/*Acaca* and FAS/*Fasn*, while downregulating mRNAs coding for FA oxidizing enzymes (Fig. 2a and Extended Data Fig. 2b, c). Liver mRNAs for inflammatory cytokines and chemokines, including TNF, were elevated (Fig. 2b). Continuous HFrD feeding dramatically increased ACC1 and FAS amounts (Fig. 2c), and upregulated hepatic DNL, elevating C16:0 and C18:0 synthesis by 2-fold relative to CSD (Fig. 2d). Short-term (48-hour) HFrD feeding, however, did not elevate FA synthesis in liver or jejunum, although it strongly increased F1P amounts in both tissues (Extended Data Fig. 2d-f). Inflammatory cytokines, chemokines, and lipogenic mRNAs, other than *Acaca,* were not induced and ACC1 protein was barely elevated after a 48-hour exposure (Extended Data Fig. 2g).

Fructose-induced barrier deterioration and intestinal epithelial ER stress

Although short term HFrD feeding did not alter intestinal permeability based on fecal albumin content and FITC-dextran translocation (Extended Data Fig. 2h), prolonged HFrD

feeding caused intestinal barrier deterioration (Fig.3a). Fecal albumin elevation, however, was prevented by treatment with an antibiotics (Abx) cocktail[21] that reduces fecal bacteria by more than 99.5% . Prolonged HFrD feeding reduced TJP mRNAs coding for Tjp2, occludin, and different claudins (including seal-forming claudin 3) in large and small intestine (Fig. 3b, c). Although some of these effects, especially in colon, were reversed by Abx treatment, most downregulated jejunal TJP mRNAs remained suppressed and occludin and claudin 1 downregulation was only partially reversed (Extended Data Fig. 3a-c), Moreover, incubation of microbiota-free colonic organoids with 5-20 mM fructose decreased numerous TJP mRNAs (Fig. 3d). *Il22* mRNA and some IL-22-induced antimicrobial protein (AMP) mRNAs (*Lcn2, S100a9*) were increased in colons of HFrD- fed mice (Extended Data Fig. 3d), presumably as an attempt at barrier restoration[22], but *Reg3b* and *Reg3g* mRNAs were suppressed by HFrD-feeding. Abx treatment attenuated *Il22*, *Lcn2*, and *S100a9* mRNA induction. Previous studies demonstrated that colonic inflammation upregulates *S100* mRNAs but downregulates *Reg* genes[23]. Administration of a 30% wt:vol fructose solution, accounting for 32% of daily caloric intake in NCD-fed BL6 mice, also reduced TJP mRNAs, caused colonic shortening and increased FITC-dextran translocation (Extended Data Fig 3e, f). In contrast, a 30% sucrose drink did not reduce colon length or TJP mRNAs and barely increased ER stress markers (Extended Data Fig.3g-i). These results are consistent with the weaker effect of sucrose vs. fructose on hepatic steatosis[24]

Colonic shortening is a sign of inflammation. To explore a plausible cause of mucosal inflammation, which can downregulate TJPs[25], we posited that the fructose metabolite F1P interferes with N-glycosylation as previously documented in hereditary fructose intolerance[26]. Defective N-glycosylation triggers ER stress, a source of mucosal inflammation[27], and impairs TJP transport and assembly[28]. Indeed, HFrD feeding strongly induced the ER stress markers/unfolded protein response (UPR) effectors *Chop*,

Bip/Grp78, and spliced *Xbp1* and increased eIF2α phosphorylation in intestinal mucosa along with elevated inflammatory markers (Fig. 3e). *In vitro* incubation of colonic organoids with fructose, but not glucose, also induced *Chop* and *sXbp1* mRNAs and this was attenuated by glucose addition (Extended Data Fig. 3j), suggesting that interference with N-glycosylation may be involved. To explore the role of F1P in this response we incubated organoids with the KHK inhibitor 420640. This abrogated *Chop* and *sXbp1* mRNA induction by fructose and diminished the decrease in most TJP mRNAs (Extended Data Fig. 3k, l). A similar protective effect was seen upon organoid incubation with the chemical chaperon tauroursodeoxycholic acid (TUDCA) (Extended Data Fig. 3m), which reduces liver ER stress and steatosis in *MUP-uPA* mice[8]. Importantly, TUDCA treatment of BL6 mice given a 30% fructose drink attenuated colonic shortening, reduced FITC-dextran translocation, inhibited ER stress marker induction and prevented TJP mRNA downregulation (Fig. 3f-h).

HFrD induces liver inflammation and myeloid cell TLR signaling

Exploratory transcriptomic analysis independently validated by immunoblot (IB) and RT-PCR analyses revealed marked differences in expression of innate immunity- and inflammation- related genes between tumor-free 6-month-old CSD- and HFrD-fed livers (Fig. 4 a, b and Extended Data Fig. 4a, b). HCC nodules, however, exhibited fewer diet-related transcriptomic changes, especially in HCC-related genes (Extended Data Fig. 4c,d), which were essentially identical to those upregulated in HFD-induced HCC[29]. HCC-specific genes were elevated in CSD- and HFrD-associated tumors from 9-month-old mice relative to non-tumor liver, further demonstrating that HFrD mainly altered hepatic pathophysiology prior to tumor onset. Gene ontology enrichment analysis of the non-tumor transcriptome revealed large changes in genes involved in response to wounding, wound healing, cell adhesion, innate immunity, and responses to molecules of bacterial origins (Extended Data Fig. 4e). IB analysis confirmed elevated TLR2 and 4, MyD88, NLRP3 and STAT3 phosphorylation in HFrD-fed livers, changes that were abrogated by Abx treatment (Fig.4c).

Increased TLR2, TLR4, MyD88 and NLRP3 expression most likely took place in liver-recruited macrophages. Accordingly, we ablated MyD88 in myeloid cells and examined the impact on HFrD-induced DNL controlling enzymes, inflammatory cytokines and hepatosteatosis. Although myeloid MyD88 ablation only inhibited *Tnf*, *Il1β* and *Ccl2* mRNA induction with no effect on *Ccl5* and *Il6* mRNAs, it substantially decreased expression of DNL-related proteins and reduced hepatic TG accumulation in HFrD-fed mice (Fig. 4d-f).

Consistent with elevated TLR expression and the protective effect of macrophage MyD88 ablation, prolonged HFrD feeding increased circulating endotoxin in *MUP-uPA* and BL6 mice, whereas Abx administration inhibited endotoxemia and attenuated HFrD-stimulated liver tumorigenesis (Extended Data Fig. 5a, b). Abx treatment also blocked hepatosteatosis, TG accumulation and induction of DNL-related enzymes, inflammatory cytokines and chemokines (Extended Data Fig. 5c-g). Importantly, Abx treatment did not reduce liver F1P and had a marginal effect on cytosolic acetyl-CoA in HFrD-fed mice (Extended Data Fig. 5h, i), suggesting it does not affect fructolysis. Abx treatment, however, prevented HFrD-induced glucose intolerance and reduced non-fasting serum insulin without affecting body or WAT weight; it also reduced liver fibrosis and abrogated colon shortening (Extended Data Fig. 5j-n).

All HFrD-elicited phenotypic changes, including hepatosteatosis and elevated DNL-related enzymes, upregulation of innate immune proteins and inflammatory mediators and downregulation of TJP genes, were also observed in 6-month-old BL6 mice and were inhibited by Abx (Extended Data Fig. 6a-g). Thus, fructose-induced barrier deterioration and subsequent DNL and steatohepatitis are independent of genetic background or carcinogen-induced genetic alterations. Fructose drink (30%) administration also enhanced hepatosteatosis and upregulated liver mRNAs encoding inflammatory chemokines, cytokines and DNL enzymes in BL6 mice (Extended Data Fig. 7a, b). Fructose drink consumption, however, increased body and WAT weight, rendering dissociation of its liver-

specific effects from those caused by increased caloric intake and peripheral obesity somewhat difficult (Extended Data Fig. 7c). To mimic human Western diet that is rich in both fat and fructose and reduce the caloric contribution of fructose from 32% in the above experiment to 20.9% an amount equivalent to that consumed by the 95th percentile of American adolescents[30], we placed BL6 mice on HFD composed of 59% fat, 15% protein and 26% carbohydrates, and either regular water or a 30% fructose drink. Despite its reduced overall caloric contribution, fructose still increased body, WAT and liver weight, augmented hepatosteatosis and induced liver mRNAs encoding inflammatory chemokines, cytokines and DNL enzymes, while downregulating TJP mRNAs and increasing FITC-dextran translocation (Extended Data Fig. 7d-h).

Barrier restoration inhibits DNL and prevents steatohepatitis

Acute tight junction loss activates YAP and TAZ, closely related transcriptional activators that stimulate tissue repair[31]. Indeed, incubation of colonic organoids with fructose rapidly induced the YAP targets *Ctgf* and *Ccne1* (Extended Data Fig. 8a). Mucosal *Ctgf* and *Ccne1* mRNAs were also upregulated in HFrD-fed mice, but this chronic response was attenuated relative to the acute response manifested by fructose-incubated organoids (Extended Data Fig. 8b). *Ccne1* encodes the matricellular protein CCN1, whose administration promotes barrier repair via integrin-mediated IL-6 incuction[32], whereas engagement of IL-6 signal transducer (IL6ST/gp130) promotes mucosal repair via STAT3 and YAP[33]. Congruently, IEC-specific expression of constitutively active gp130 variant (gp130[Act])[33] conferred partial resistance to fructose-induced TJP mRNA downregulation in organoids (Extended Data Fig. 8c). IEC- specific gp130[Act] expression was even more effective *in vivo*, restoring *Reg3b*, *Reg3g*, Tjp mRNAs and claudin-1 and inhibiting HFrD-induced FITC-dextran translocation and endotoxemia (Extended Data Fig. 8d-h). Remarkably, *MUP-uPA/gp130[Act]* mice were resistant to fructose-induced hepatic tumorigenesis and failed to upregulate hepatic mRNAs

encoding inflammatory and lipogenic proteins (Fig. 5a, b). Liver DNL rates were lower in HFrD-fed *MUP-uPA/gp130^{Act}* mice than in *MUP-uPA* mice (Fig. 5c), but F1P accumulation in either liver or jejunum was not reduced (Extended Data Fig. 8i), indicating that YAP and STAT3 activation does not decrease fructose uptake. Administration of recombinant CCN1 was also protective, reversing fructose-induced colon-shortening and TJP mRNA downregulation and reducing fecal albumin (Extended Data Fig. 8j-l). Moreover, CCN1 treatment inhibited fructose-stimulated DNL, hepatosteatosis, steatohepatitis and liver FAS expression without affecting body weight (Extended Data Fig. 8m-p).

Reg3β, whose expression is suppressed by HFrD, is an AMP that targets gram-negative bacteria and may neutralize endotoxin[34]. Accordingly, transgenic Reg3β expression from the IEC-specific *Villin* promoter prevented HFrD-induced hepatosteatosis (Fig. 5d). The *Reg3b* transgene also prevented fructose induction of liver mRNAs for inflammatory cytokines and lipogenic enzymes without affecting body weight (Fig. 5e, f). Reg3β IEC expression reduced HFrD-induced endotoxemia, but the increase in circulating endotoxin in HFrD-fed wt animals was of low statistical significance (Extended Data Fig. 8q). Conversely, low-dose LPS administration for 3 months caused TG accumulation and upregulation of DNL- and inflammation-related mRNAs in both CSD-fed *MUP-uPA* and HFrD-fed *MUP- uPA/gp130^{Act}* livers (Extended Data Fig. 9a-f), suggesting that circulating endotoxin triggers fatty liver disease.

Sequencing of fecal microbial 16S rRNA gene amplicons confirmed that prolonged HFrD consumption caused mild dysbiosis in *MUP-uPA* mice, characterized by decreased α diversity (Extended Data Fig. 9g). β diversity analysis by PERMANOVA based on unweighted UniFrac distances revealed significant (pseudo-*F* statistic = 2.88, *P* < 0.001) clustering of fecal samples according to diet (Extended Data Fig. 9h). Fecal 16S sequencing on CSD- and HFrD-fed *MUP-uPA/gp130^{Act}* mice showed that prolonged HFrD feeding also caused dysbiosis in this mouse strain (Extended Data Fig. 9i, j).

TNF stimulates fructose-driven lipogenesis

We used primary hepatocyte cultures to examine whether TNF also stimulates fructose-driven steatosis in human liver. Primary hepatocytes from healthy donors were left unstimulated or treated with either LPS or TNF and placed in sugar-free culture medium or medium containing 5 mM glucose or fructose for 48 hours, after which lipid droplet accumulation was assessed. Whereas glucose or fructose alone or together with LPS barely affected lipid droplet formation, TNF treatment strongly enhanced lipid droplet buildup in both fructose and glucose incubated hepatocytes (Fig. 6a, b). TNF, but not LPS, induced *ACACA*, *FASN* and *SREBF1* mRNAs.

Discussion

Excessive fructose intake causes dysbiosis and TJP downregulation, resulting in intestinal barrier deterioration and low-grade endotoxemia[11–13]. Fructose consumption stimulates hepatosteatosis and when combined with other risk factors can cause steatohepatitis and even HCC. It is well established that fructose is a more effective inducer of hepatic DNL than glucose[19,20]. However, the exact mechanism by which fructose preferentially stimulates DNL, other than its KHK-dependent conversion to acetyl-CoA via fructolysis, remains obscure. In particular, the metabolic effects of fructose-induced barrier deterioration and endotoxemia have not been investigated. We now show that fructose-induced endotoxemia, which can be prevented through transgenic gp130 and Reg3β expression or CCN1 administration, activates MyD88-mediated inflammatory signaling in liver myeloid cells, thus leading to TNF induction (Fig. 6c). We previously showed that TNF signaling via TNFR1 together with ER stress-activated IRE1 stimulates hepatosteatosis through caspase-2 mediated SREBP1 activation[9]. Accordingly, myeloid cell MyD88 signaling is required for induction of the key lipogenic enzymes ACC1 and FAS in mouse liver and TNF treatment of cultured human hepatocytes greatly enhances lipid droplet buildup after incubation with either fructose or glucose, correlating with *SREBF1, ACACA*

and *FASN* mRNA induction. Of note, fructose-induced endotoxemia does not affect fructose uptake, its conversion to F1P and subsequent acetyl-CoA generation via fructolysis. These new insights to fructose-induced hepatic lipid accumulation suggest that fructose and other dietary factors that cause barrier deterioration contribute to the onset of steatohepatitis by stimulating net FA and TG accumulation in hepatocytes and also by decreasing mitochondrial β oxidation.

Our results explain why fructose rather than glucose leads to barrier deterioration. Fructose is converted by KHK to F1P, a toxic metabolite whose accumulation in aldolase B deficient individuals interferes with protein N-glycosylation[26]. Defective N-glycosylation interferes with protein transport and secretion, thereby leading to ER stress and inflammation[35]. We show that HFrD, but not CSD, consumption induces ER stress in IEC and colonic inflammation. Fructose treatment of colonic organoids also triggers ER stress, which can be prevented by KHK inhibition. In addition to inflammation, ER stress also causes TJP downregulation[27,28], increasing translocation of luminal microbial products and enhancing the hepatic inflammatory response. Accordingly, the chemical chaperon TUDCA, activation of mucosal-regenerative gp130 signaling or administration of CCN1 prevent fructose-induced TJP downregulation and endotoxemia, thus blocking subsequent stimulation of hepatic DNL and steatohepatitis (Fig.6c).Future studies will tell whether CCN1 and other agents, such as aryl hydrocarbon receptor agonists[36], that stimulate mucosal healing can reduce NAFLD and NASH incidence in humans. Another potential preventative/therapeutic approach that deserves further consideration is endotoxin neutralization. Although our mouse model experiments, which employ high amounts of fructose, may not be immediately extended to humans, we suggest that barrier deterioration may only occur after continuous and excessive consumption of fructose and is probably influenced by various dietary and genetic factors or co-morbidities. Of note, the composition of the diet determines the relative contribution of DNL to hepatosteatosis, such that DNL

becomes more important when fat intake is low. Nonetheless, barrier decline has been described in various experimental models and in numerous liver diseases that entail hepatic fat accumulation and inflammation[37,38]. Thus, the finding that excessive fructose ingestion leads to hepatic fat accumulation through a pathway that involves barrier deterioration, endotoxemia, activation of myeloid cell MyD88 signaling and TNF secretion, and induction of lipogenic enzymes in hepatocytes, may be of relevance to several common liver diseases and metabolic disorders.

Methods

Mouse Studies

   MUP-uPA and *gp130^Act* mice were described[8,33] and were crossed to generate *MUP-uPA/gp130^Act* mice. C57BL/6 mice were purchased from Charles River Laboratories and *Reg3b^IEC* transgenic mice in which the *villin* promoter drives *Reg3b* in intestinal epithelial cells (IEC) were generated at the University of Frankfurt. All experiments were conducted on adult males, whose age is specified in the Figure Legends and Method Details section. To induce HCC in BL6 mice, DEN (25 mg/kg) was injected intraperitoneally (i.p.) into 14-day-old males. Mice were randomly placed on one of two isocaloric diets purchased from Research Diets Inc.: (a) control corn starch diet (CSD) in which 70% of calories are from corn starch, 10% from fat, and 20% from protein, totaling 4.1 kcal/g, or (b) high-fructose diet (HFrD) in which 60 % of calories are from fructose, 10% from corn starch, 10% from fat, and 20% from protein; 4.1 kcal/g. Both diets contain 4.7 gm % fiber. Mice were treated with antibiotics as described[21,39]. Mice were also given NCD or HFD as previously[8] and allowed free access to either 30% fructose or sucrose in water solution or regular drinking water. Mice were given daily 250 mg/kg TUDCA or vehicle (PBS) i.p. injections for the last 10 weeks of fructose drink exposure. All mice, unless indicated otherwise, were on the C57BL/6 background and group-housed (3-4 mice per cage) in filter-topped cages on autoclaved food and water at UCSD, according to NIH guidelines. All experiments were

performed using UCSD IACUC-approved protocols in accordance with UCSD and NIH guidelines and regulations. The *Reg3b^{IEC}* experiments were performed at the University of Frankfurt in accordance with German law and regulations.

Human Hepatocyte Cultures

Donor livers rejected for transplantation were obtained via LifeSharing OPO as a part of Dr.T. Kisseleva's research program. Donors with no history of alcohol abuse, low BMI (18-22), no liver fibrosis, no diabetes, minimal steatosis, and normal levels of ALT and AST were qualified as normal in this study conducted under **IRB 171883XX (approved on 11/9/17**). For hepatocyte isolation the livers were placed on top of an ice pan covered by a plastic bag and then a sterile field. Catheters were inserted into the major portal and/or hepatic vessels and the tissue was perfused with cold organ preservation solution or EMEM (Corning Cellgro cat # 15-010-CM) + 25 mM HEPES (Corning Cellgro cat# 25-060-CI) to determine which vessels provide the most uniform tissue perfusion. This step also helps remove any remaining blood. The catheters were then secured into the vessels either by sutures or surgical grade glue. All remaining major vessels on the cut surfaces were closed with sutures or surgical grade glue. The liver tissue was then placed in a sterile plastic bag and connected to a peristaltic pump with flowrate dependent on the number of catheters and size of tissue.

The bag containing the tissue was placed in a water bath at 38.5°C and the tissue was perfused with HBSS (without calcium and magnesium or phenol red) (Hyclone cat # SH30588.02) supplemented with 1.0 mM EGTA without recirculation for 10-20 min. The EGTA chelates calcium which leads to the separation of cell junctions and helps remove any residual blood. Finally, the liver specimen was perfused with EMEM containing 0.1 mg/ml of collagenase (VitaCyte cat# 001-2030) and 0.02 mg/ml of protease (VitaCyte cat# 003-1000) which is recirculated as long as needed to complete the digestion (15-30 min total digestion time). Perfusion was stopped when the

liver tissue began to show fissures and separation from the liver capsule. The liver tissue was then removed from the plastic bag and placed in a sterile plastic beaker that contains warmed (37°C) DMEM supplemented with 5% FBS, 1% Sodium pyruvate, 1% antibiotic. The specimen was then gently dissociated with sterile scissors to release hepatocytes. The cell suspension was filtered through sterile nylon mesh covered funnels to remove cellular debris and clumps of undigested tissue. The above steps were repeated as many times as needed to obtain the maximum numbers of cells. Hepatocytes were isolated from other cell types in the suspension by low speed centrifugation at 80x g for 5 min at 18°C. The supernatant was decanted and saved (NPC fraction).The hepatocyte pellets were gently resuspended in a Percoll (Sigma # GE17-0891-09) gradient and centrifuged at 100x g for 10 minutes at 18°C.The supernatant was removed by aspiration and the pellets were saved and resuspended in warmed (37°C) DMEM and the centrifugation step was repeated. The supernatant was removed and the hepatocytes were resuspended in 4°C Hypothermosol FRS (BioLIfe Solutions # 101104) to make the Hepatocyte Stock. An aliquot of the Hepatocyte Stock (150 µl) was removed and placed in a 1.5ml Eppendorf tube, mixed with an equal volume of trypan blue and assessed by dye exclusion to determine cell viability and number using a hemocytometer. Cell viability was expressed as a percentage of the total cells counted (# of live cells/[# of live cells + # of dead cells] x 100 = % viable). Usually there were $515X10^6$ total viable cells in the Hepatocyte Stock. An aliquot of $6X10^6$ viable hepatocytes was removed from the hepatocyte stock and diluted with 5 volumes of ice cold EMEM. The aliquot was centrifuged at 100x g and 18^0C for 5 min. The supernatant was removed and the pellet was resuspended in 12 ml of Hepatocyte Plating Medium[**]. The hepatocytes were then seeded on a collagen coated 24 well plate and allowed to attach in a 37^0C, 5% CO2 incubator for 2-12 hours and then the medium is changed to serum free Hepatocyte Maintenance Medium. The remaining Hepatocyte Stock was allowed to settle at 4°C for 1-2 hours. The excess liquid was carefully removed from the bottle with care not to disturb the hepatocytes at the bottom. The cell suspension was then brought to a final concentration of 8×10^6 hepatocytes/ml using a solution of Cryostor

CS10 (BioLife Solutions # 210102) +DMSO+Fructose giving a final concentration of 10% DMSO + 100 mM Fructose. The cell suspension was placed at 1.5ml/vial, into 2ml freezing vials and frozen in control rate freezer till used.

*Hepatocyte Plating Medium: Williams' E medium from Life Technologies (Cat. # A12176-01) containing 10mM HEPES, 2mM L-Glutamine, 10%FBS, 1X10-7M Dexamethasone, 1X10-7M Insulin and 1% Antibiotic/Antimycotic solution. **Hepatocyte Maintenance Medium = Hepatocyte Plating Medium without FBS

Histology

Freshly collected liver tissues from *MUP-uPA, MUP-uPA;gp130[Act], Reg3b[IEC]* and C57BL/6 mice were fixed in 10% neutral-buffered formalin or 4% paraformaldehyde, embedded in paraffin, sectioned and stained with hematoxylin and eosin (H&E) and Sirius Red. For frozen-block preparation, tissues were embedded in Tissue-Tek OCT compound and stained with Oil Red O and H&E. For Oil Red O and Sirius Red analysis, multiple images were examined for each section. Representative images were captured on an upright light/fluorescent microscope (Zeiss) equipped with an AxioCam camera.

Lipidomics

Triacylglycerol (TAG) lipid species were measured as described[40] with minor modifications. Briefly, freshly isolated liver samples were homogenized in one volume of phosphate buffered saline (PBS) (pH 7.4), and sonicated. Next, a BCA protein assay was performed and 25 µg of each liver sample aliquoted and utilized for lipid extraction. An internal standard mixture and $CHCl_3$/methanol (2:1) mixture were added to each sample before being vortexed, mixed, sonicated, and centrifuged. Lipid-containing supernatants were removed and dried before being resuspended in H_2O-saturated butanol and sonicated again. Methanol with 10 mM ammonium were added and the resuspended samples were

centrifuged and the supernatants were transferred to individual glass vials. Lipidomic

determination was performed by liquid chromatography electrospray ionization tandem

mass spectrometry (LC-MS) combined with a triple quadrupole mass spectrometer. Data

were analyzed using Multiquant software v1.2 and TAG normalized to the total

phosphatidylcholine (PC) levels of each sample.

Indirect calorimetry

Mice were placed into Comprehensive Lab Animal Monitoring System (CLAMS;

Columbus Instruments) metabolic cages to adapt to their surroundings for 48 hours before

study. Data from 3 light/dark cycles were used in the analysis. Rates of O_2 consumption

(VO_2; ml/kg/hour) and CO_2 production (VCO_2) were continuously acquired.

Immunoblotting and antibodies

IB analysis was performed on tissue or cell lysates that were SDS-PAGE separated and

transferred to nitrocellulose membranes. Blots were incubated with 5% (wt:vol) nonfat dry

milk in PBS with 0.05% (wt:vol) Tween 20 (Millipore Sigma) (PBST) at room temperature for

1 hour to block nonspecific binding, and overnight at 4° C with primary antibodies in 3%

BSA (wt:vol) in PBST and finally with HRP-conjugated secondary antibody in blocking

buffer. Blots were developed using the Western Lightning Plus-ECL enhanced

chemiluminescence detection kit (PerkinElmer). Immunoblotting was performed with

antibodies against TLR2 (Santa Cruz, sc-21760), TLR4 (Santa Cruz, sc-293072), MyD88

(Santa Cruz, sc-74532), phospho-STAT3 (Cell Signaling, CS9145), STAT3 (Cell Signaling,

CS12640), NLRP3 (LSBio, LS- C334192), FAS (Cell Signaling, #3180), ACC (Cell

Signaling, #3662), ERK1/2 (Cell Signaling, #9102), Occludin (Santa Cruz, sc-271842) and

Claudin 1 (Santa Cruz, sc- 166338).

Glucose tolerance test

Mice were transferred to clean cages with no food and fasted for approximately 12 hours

with access to drinking water. A 20% glucose solution was i.p. injected (2 g/kg mouse body

mass) and small drops of blood were obtained from tail cuts and assessed for baseline glucose levels using a One-touch Ultra 2 (Lifescan, Johnson & Johnson) glucometer at 30, 60, 90 and 120 minutes.

Intestinal permeability

Fecal albumin measurements were performed on dried fecal pellets using the Mouse Albumin ELISA Quantitation Set from Bethyl Laboratories according to manufacturer's instructions. An *in vivo* permeability assay to assess barrier function was performed using the FITC-labeled dextran method. Food and water were withdrawn overnight, and mice were gavaged with 45 mg/100 g body weight of FITC-labeled dextran (FD-4; Sigma-Aldrich). Serum was collected 5 hours after FD-4 gavage, and fluorescence intensity of each sample was measured (excitation, 492 nm; emission, 525 nm). Serum or plasma LPS concentrations were determined with the Mouse Lipopolysaccharides (LPS) ELISA Kit obtained from Cusabio following manufacturer's instructions.

Cytosolic acetyl-CoA measurement

Frozen liver pieces were weighed, thawed, cut into smaller pieces and homogenized using a pestle in 1.5 ml microfuge tubes on ice. The cytoplasmic fraction was separated from the mitochondria and deproteinized using Mitochondria/Cytosol Fractionation Kit (Bio Vision, # K256) and Deproteinizing Sample Preparation Kit (Bio Vision, # K808), respectively. Acetyl-CoA concentrations were determined using PicoProbe™ Acetyl-CoA Assay Kit (Bio Vision, #K317).

Intestinal organoid culture

Intestinal crypts were isolated from *MUP-uPA* and *gp130^Act* mouse colons and were cultured as described[41]. Two days after passaging, when the crypts started budding, the medium was changed to DMEM (Gibco, 11966-025) supplemented with 5 mM or 20 mM glucose or fructose or a combination of both sugars (5 mM glucose and 20 mM fructose) and 10% FBS. After changing the medium, the organoids were cultured for 24 hours.

RNA-seq analysis

RNA was extracted from snap-frozen liver using the NucleoSpin® RNA kit (Macherey-Nagel) according to manufacturer's instructions. Library preparation for RNA-seq was performed using TruSeq Stranded mRNA Library Prep Kit (Illumina) following manufacturer's guidelines and best practices. For quality control of the libraries, the samples were inspected with a Bioanalyzer chip (DNA 1000, Agilent). Sequencing was performed for paired-end samples on a HiSeq 2500 v4.0 system. The resulting fastq files were quality controlled using FastQC, and adapters were trimmed using TrimGalore! v0.4.0 (both developed at The Babraham Institute) for paired-end sequenced samples. The trimmed fastq files were aligned to the mouse reference genome (Mus_musculus.GRCm38.83) using STAR aligner (v2.5.1) [42]. RSEM (v1.3.0)[43] was used to estimate gene expression levels. Downstream analysis for differential gene expression of the raw count table was performed using DESeq2[44] in R. Heatmaps were drawn using the R package pheatmap (Pretty Heatmaps; R package version 1.0.10; https://CRAN.R-project.org/package=pheatmap) clustering columns and rows and the values for each row being centered and scaled. Mapping of gene expression levels to corresponding KEGG pathways was performed using the R packages gage[45] and path view[46].

Quantitative real-time PCR analysis

RNA samples were prepared using RNeasy kit (Qiagen). RNA was reverse transcribed using a Super Script VILO cDNA synthesis kit (Thermo Scientific) and qPCR was performed using SYBR green (Biorad) based real-time PCR on a Biorad CFX96 machine. Relative mRNA expression was calculated from the comparative threshold cycle (Ct) values relative to ribosomal protein S18 mRNA. PCR primers were designed using online primer tools Primer3Plus and purchased from Integrated DNA Technologies. Primer sequences are provided in table S1.

Microbiome analysis

Samples were processed following the Earth Microbiome Project[47] DNA extraction and 16S rRNA gene amplicon sequencing protocol, updated for the Kingfisher liquid-handling robot[48]. In brief, the 96-well MoBio Powersoil DNA kit was used to extract DNA from fecal samples and barcoded 515F-806R primers targeting the V4 region of the 16S rRNA were used for 16S amplification. Sequencing was performed at UCSD Institute for Genomic Medicine (IGM) on an Illumina MiSeq. 16S sequencing data were   uploaded to Qiita (https://qiita.ucsd.edu/) for QC, demultiplexing and processing with Deblur[49]. The resulting deblurred feature table was downloaded for analysis with QIIME 2 (https://qiime2.org) v 2017.10[50]. The feature table was rarified to 8150 sequences per sample and the rarified table used for alpha diversity and beta diversity analysis. Taxonomic assignment was performed with QIIME 2 using a naive bayes sklearn classifier trained on the 515F/806R region of Greengenes 13_8 99% OTUs.

D_2O administration and measurement of *de novo* lipogenesis

MUP-uPA and *MUP-uPA/gp130^{Act}* mice were fed *ad libitum* CSD or HFrD for either 12 weeks or 48 hours from 6-8 weeks of age. One day before termination, mice were i.p. injected with 0.028 ml/g body weight 0.9% NaCl D_2O, and drinking water was replaced with 6% D_2O-enriched water. 19-20 hours later, plasma and tissue samples were immediately snap-frozen in liquid nitrogen.

The ^2H labeling of water from samples or standards was determined by deuterium acetone exchange. 5 µl of sample or standard were reacted with 4 µl of 10 M NaOH and 4 µl of a 5% (vol:vol) solution of acetone in acetonitrile for 24 hours. Acetone was extracted by addition of 600 µl chloroform and 0.5 g Na_2SO_4 followed by vigorous mixing. 80 µl of the chloroform was then transferred to a glass GC–MS vial. Acetone was measured using an Agilent DB-35MS column (30 m x 0.25 mm i.d. x 0.25 µm, Agilent J&W Scientific) installed mass spectrometer (MS) with the following temperature program: 60° C initial, increase by 20° C/min to 100° C, increase by 50° C/min to 220° C, and hold for 1 minute. The split ratio

was 40:1 with a helium flow of 1 ml/min. Acetone eluted at approximately 1.5 minutes. The

mass spectrometer was operated in the electron impact mode (70 eV). The mass ions 58,

59, and 60 were integrated and the percent M1 and M2 (m/z 59 and 60) calculated. Known

standards were used to generate a standard curve and plasma percent enrichment was

determined from this. All samples were analyzed in triplicate. *In vivo* calculation of the

fraction of newly synthesized fatty acids (FNS) was based on the method described in[51]

where FNS is described by the following equation: $FNS = \frac{ME}{(n \times p)}$ where ME is the average

number of deuterium atoms incorporated per molecule (ME = 1 × m_1 + 2 × m_2 + 3 × m_3...),

p is the deuterium enrichment in water and *n* is the maximum number of hydrogen atoms

from water incorporated per molecule. *n* was determined using the equation: $\frac{m_2}{m_1} = \frac{(n-1)}{2} \times \frac{p}{q}$,

as described in[51], where q is the fraction of hydrogen atoms and p + q = 1.

GC–MS analysis of fatty acids and polar metabolites

For tissue and plasma, total fatty acids were extracted from tissues and plasma using a

Folch-based methanol/chloroform/saline extraction at a ratio of 1:2:1 with inclusion of 10

nmol/mg [^{2}H$_{31}$]palmitate as a lipid internal standard as described previously[52]. Briefly, 250 µl

methanol, 500 µl chloroform, 250 µl saline and isotope internal standards were added to

~20 mg weighed tissue in a 2 mL Eppendorf. This was pulverized in a Retsch mill with 3 ball

bearings for 5 minutes followed by removal of ball bearings and centrifugation at 21,000 g

for 10 minutes. The lower chloroform phase was dried and then derivatized to form fatty

acid methyl esters (FAMEs) via addition of 500 µl 2% H_2SO_4 in MeOH and incubation at 50°

C for 2 hours. FAMEs were extracted via addition of 100 µl saturated salt solution and 2

successive additions of 500 µl hexane and these were analyzed using a Select FAME

column (100 m x 0.25 mm i.d.) installed in an Agilent 7890A GC interfaced with an Agilent

5975C MS using the following temperature program: 80° C initial, increase by 20° C/min to

170° C, increase by 1° C/min to 204° C, then 20° C/min to 250° C and hold for 10 minutes.

The percent isotopologue distribution of each fatty acid was determined and corrected for natural abundance.

F1P analysis in liver and intestine

<u>Materials</u>

Optima LC/MS grade water was sourced from Fisher Scientific (Part number: W6-4). Pure HPLC ethyl alcohol was purchased from Sigma-Aldrich (Part number: 459828-2L). HPLC grade acetonitrile, methanol, and isopropyl alcohol were purchased from Honeywell (Part numbers: LC015-4, LC230-4, and LC323-4).

<u>Sample Prep</u>

Pre-weighed frozen tissue was transferred to a pre-chilled 2 mL homogenization tube containing 300 mg of 1 mm zirconium disruption beads. To each sample, a -20° C mixture of methanol:water (1:1) was added to achieve a normalized concentration of 50 µg of tissue per 1 µL of solvent. The samples were then homogenized using a BeadRuptor Elite homogenizer at a speed of 8 m/s for 3 cycles involving 10 seconds of homogenization followed by 10 seconds of dwell. The samples were then immediately placed on dry ice and the homogenate was transferred to clean 1.5 mL microfuge tubes and allowed to deproteinize for 30 minutes at -20° C. Samples were then centrifuged at a speed of 14,000 rpm at 4° C for 10 minutes. 50 µL of each sample's supernatant was then transferred to an amber autosampler vial containing a Wheaton 300 µL glass insert. Samples were stored in an Agilent Infinity 1290 UHPLC Autosampler maintained at 4° C until 20 µL of each sample was injected for targeted analysis by LC-MS/MS.

<u>LC-MS/MS Data Acquisition</u>

Chromatographic separation was performed on an Agilent Infinity 1290 UHPLC equipped with a Shodex HILICpak VT-50 2D Column (100 Å, 5 µm particle size, 2.0 x 150 mm, P/N SH-F7630400) maintained at a temperature of 60° C. Elution was performed with an isocratic elution of mobile phase containing 80:20 water:acetonitrile with 25 mM ammonium

formate at a constant flow rate of 0.250 mL/min over the course of 14 minutes. Data acquisition was performed on an Agilent 6495 Triple Quadrupole Mass Spectrometer equipped with an Agilent Jet Stream electrospray ionization source operating in negative mode under the following source settings: Gas Temp 200° C; Gas Flow 11 l/min; Nebulizer 35 psi; Sheath Gas Temp 400° C; Sheath gas flow 11 l/min; Capillary voltage 3000 V; Nozzle Voltage 1500 V; High Pressure RF 50 V; Low Pressure RF 40 V. Fructose-1-phosphate was monitored using a single MRM with the following settings:

Analytes	Retention Time (min)	Precursor Ion	Product Ion	Dwell	Fragment or	Collision Energy	Cell Accelerator Voltage
Fructose 1 Phosphate	8.41	259.02	259.02	200	380	0	5

In vivo treatment with LPS

Six-week-old *MUP-uPA* and *MUP-uPA/gp130^Act^* mice were fed CSD or HFrD diet and i.p. injected daily with LPS (*E. coli*, Sigma Chemical, St. Louis, MO; 0.25 mg/kg) or vehicle (PBS). The mice were sacrificed after twelve weeks of treatment and the tissues were collected for further analysis.

In vivo treatment with CCN1

Recombinant CCN1 was purified as described[53]. Six-week-old *MUP-uPA* mice were fed HFrD for twelve weeks and i.p. injected with vehicle or 2 ug CCN1 in 200 µl of PBS every other day for the last four weeks of the experiment. The mice were sacrificed at 18 weeks of age and the tissues were collected for further analysis.

Quantification and Statistical Analysis

Data are presented either as means ± SEM or medians of continuous values and were analyzed by an unpaired two-sided Students' *t*-test or Mann–Whitney test for comparison of two groups, respectively, followed by Benjamini-Hochberg FDR adjustment for *P*-values. Statistical significance is defined as a *P*-value greater than 0.05. Significance testing for differentially abundant bacteria was performed with the QIIME2 implementation of ANCOM[54].

Author Contributions

J.T. designed the project, performed most experiments, analyzed data and wrote the paper

with M.K., who conceived and supervised the project; G.D.C. performed major experiments; S.R. performed and analyzed RNA-Seq data; D.C.H. and P.M. performed lipidomic studies; C.R.G. and C.M.M. designed and conducted DNL measurements; A.V. and R.K. conducted microbiome analysis and contributed to writing; K.T. generated $gp130^{Act}$ mice; F.C., C.C. and F.R.G. generated and analyzed $Reg3b^{IEC}$ mice; L.L. produced recombinant CCN1; S.S. performed DSS treatment and tissue and data analysis. R.M. performed further experiments. J.M. and M.T.D.-M. supervised metabolomic studies; M.A.F. designed and supervised RNA-Seq and lipidomic studies. X.L. and T.K. provided human hepatocytes, J.D.W., R.M., M.N. and M.J. planned, optimized and performed fructose metabolite measures. All authors reviewed the manuscript.

Competing Interests Statement

M.K. holds a US patent on the use of *MUP-uPA* mice to study NASH and HCC (10,034,462 B2). All other authors declare no competing interests.

Data Availability

RNA-Seq data are deposited in NCBI Gene Expression Omnibus (GEO) database under accession number GSE119080. Microbiome sequencing data are deposited in EMBL-EBI under accession number ERP110352.

References

1. Spengler, E. K. & Loomba, R. Recommendations for Diagnosis, Referral for Liver Biopsy, and Treatment of Nonalcoholic Fatty Liver Disease and Nonalcoholic Steatohepatitis. *Mayo Clin Proc* **90**, 1233–1246 (2015).

2. Stickel, F. & Hellerbrand, C. Non-alcoholic fatty liver disease as a risk factor for hepatocellular carcinoma: mechanisms and implications. *Gut* **59**, 1303–7 (2010).

3. Tilg, H. & Moschen, A. R. Evolution of inflammation in nonalcoholic fatty liver disease: the multiple parallel hits hypothesis. *Hepatology* **52**, 1836–1846 (2010).

4.   Fukui, H. Increased Intestinal Permeability and Decreased Barrier Function: Does It Really Influence the Risk of Inflammation? *Inflamm. Intest. Dis.* **1**, 135–145 (2016).

5.   Lebeaupin, C. *et al.* Endoplasmic reticulum stress signalling and the pathogenesis of non-alcoholic fatty liver disease. *J. Hepatol.* **69**, 927–947 (2018).

6.   Puri, P. *et al.* Activation and Dysregulation of the Unfolded Protein Response in Nonalcoholic Fatty Liver Disease. *Gastroenterology* **134**, 568–576 (2008).

7.   Rahman, K. *et al.* Loss of Junctional Adhesion Molecule A Promotes Severe Steatohepatitis in Mice on a Diet High in Saturated Fat, Fructose, and Cholesterol. *Gastroenterology* **151**, 733-746.e12 (2016).

8.   Nakagawa, H. *et al.* ER stress cooperates with hypernutrition to trigger TNF-dependent spontaneous HCC development. *Cancer Cell* **26**, 331–343 (2014).

9.   Kim, J. Y. *et al.* ER Stress Drives Lipogenesis and Steatohepatitis via Caspase-2 Activation of S1P. *Cell* **175**, 133-145.e15 (2018).

10.   Vos, M. B. & Lavine, J. E. Dietary fructose in nonalcoholic fatty liver disease. *Hepatology* **57**, 2525–2531 (2013).

11.   Jin, R. *et al.* Fructose induced endotoxemia in pediatric nonalcoholic Fatty liver disease. *Int J Hepatol* **2014**, 560620 (2014).

12.   Kavanagh, K. *et al.* Dietary fructose induces endotoxemia and hepatic injury in calorically controlled primates. *Am J Clin Nutr* **98**, 349–357 (2013).

13.   Spruss, A., Kanuri, G., Stahl, C., Bischoff, S. C. & Bergheim, I. Metformin protects against the development of fructose-induced steatosis in mice: role of the intestinal barrier function. *Lab. Investig.* **92**, 1020–1032 (2012).

14.   Lambertz, J., Weiskirchen, S., Landert, S. & Weiskirchen, R. Fructose: A Dietary Sugar in Crosstalk with Microbiota Contributing to the Development and Progression of Non-Alcoholic Liver Disease. *Front Immunol* **8**, 1159 (2017).

15.   Oh, J.-H. *et al.* Dietary Fructose and Microbiota-Derived Short-Chain Fatty Acids

Promote Bacteriophage Production in the Gut Symbiont Lactobacillus reuteri. *Cell Host Microbe* **25**, 273-284.e6 (2019).

16. Chang, P. V, Hao, L., Offermanns, S. & Medzhitov, R. The microbial metabolite butyrate regulates intestinal macrophage function via histone deacetylase inhibition. *Proc. Natl. Acad. Sci. U. S. A.* **111**, 2247–52 (2014).

17. Kelly, C. J. *et al.* Crosstalk between Microbiota-Derived Short-Chain Fatty Acids and Intestinal Epithelial HIF Augments Tissue Barrier Function. *Cell Host Microbe* **17**, 662–71 (2015).

18. Geidl-Flueck, B. & Gerber, P. A. Insights into the Hexose Liver Metabolism-Glucose versus Fructose. *Nutrients* **9**, 1026 (2017).

19. Softic, S., Cohen, D. E. & Kahn, C. R. Role of Dietary Fructose and Hepatic De Novo Lipogenesis in Fatty Liver Disease. *Dig Dis Sci* **61**, 1282–1293 (2016).

20. Softic, S. *et al.* Divergent effects of glucose and fructose on hepatic lipogenesis and insulin signaling. *J. Clin. Invest.* **127**, 4059–4074 (2017).

21. Grivennikov, S. I. *et al.* Adenoma-linked barrier defects and microbial products drive IL-23/IL-17-mediated tumour growth. *Nature* **491**, 254–8 (2012).

22. Karin, M. & Clevers, H. Reparative inflammation takes charge of tissue regeneration. *Nature* **529**, 307–315 (2016).

23. Barnett, M. P. G. *et al.* Changes in colon gene expression associated with increased colon inflammation in interleukin-10 gene-deficient mice inoculated with Enterococcus species. *BMC Immunol.* **11**, 39 (2010).

24. Siddiqui, R. A. *et al.* Comparative study of the modulation of fructose/sucrose-induced hepatic steatosis by mixed lipid formulations varying in unsaturated fatty acid content. *Nutr. Metab. (Lond).* **12**, 41 (2015).

25. Landy, J. *et al.* Tight junctions in inflammatory bowel diseases and inflammatory bowel disease associated colorectal cancer. *World J. Gastroenterol.* **22**, 3117–3126

(2016).

26.   Jaeken, J., Pirard, M., Adamowicz, M., Pronicka, E. & van Schaftingen, E. Inhibition of phosphomannose isomerase by fructose 1-phosphate: an explanation for defective N-glycosylation in hereditary fructose intolerance. *Pediatr. Res.* **40**, 764–6 (1996).

27.   Kaser, A. & Blumberg, R. S. Endoplasmic reticulum stress and intestinal inflammation. *Mucosal Immunol.* **3**, 11–6 (2010).

28.   Balda, M. S. & Matter, K. Tight junctions. *J. Cell Sci.* **111 (Pt 5)**, 541–7 (1998).

29.   Shalapour, S. *et al.* Inflammation-induced IgA+ cells dismantle anti-liver cancer immunity. *Nature* **551**, 340–345 (2017).

30.   Vos, M. B., Kimmons, J. E., Gillespie, C., Welsh, J. & Blanck, H. M. Dietary fructose consumption among US children and adults: the Third National Health and Nutrition Examination Survey. *Medscape J. Med.* **10**, 160 (2008).

31.   Low, B. C. *et al.* YAP/TAZ as mechanosensors and mechanotransducers in regulating organ size and tumor growth. *FEBS Lett* **588**, 2663–2670 (2014).

32.   Choi, J. S., Kim, K.-H. & Lau, L. F. The matricellular protein CCN1 promotes mucosal healing in murine colitis through IL-6. *Mucosal Immunol.* **8**, 1285–1296 (2015).

33.   Taniguchi, K. *et al.* A gp130–Src–YAP module links inflammation to epithelial regeneration. *Nature* **519**, 57–62 (2015).

34.   Miki, T., Holst, O. & Hardt, W.-D. The bactericidal activity of the C-type lectin RegIIIβ against Gram-negative bacteria involves binding to lipid A. *J. Biol. Chem.* **287**, 34844–55 (2012).

35.   Schröder, M. & Kaufman, R. J. ER stress and the unfolded protein response. *Mutation Research - Fundamental and Molecular Mechanisms of Mutagenesis* vol. 569 29–63 (2005).

36.   Metidji, A. *et al.* The Environmental Sensor AHR Protects from Inflammatory Damage

by Maintaining Intestinal Stem Cell Homeostasis and Barrier Integrity. *Immunity* **49**, 353-362.e5 (2018).

37.   Fukui, H. Increased Intestinal Permeability and Decreased Barrier Function: Does It Really Influence the Risk of Inflammation? *Inflamm. Intest. Dis.* **1**, 135–145 (2016).

38.   Wiest, R., Albillos, A., Trauner, M., Bajaj, J. S. & Jalan, R. Targeting the gut-liver axis in liver disease. *J. Hepatol.* **67**, 1084–1103 (2017).

39.   Ammirante, M., Luo, J.-L., Grivennikov, S., Nedospasov, S. & Karin, M. B-cell-derived lymphotoxin promotes castration-resistant prostate cancer. *Nature* **464**, 302–305 (2010).

40.   Fu, S. *et al.* Polysome profiling in liver identifies dynamic regulation of endoplasmic reticulum translatome by obesity and fasting. *PLoS Genet* **8**, e1002902 (2012).

41.   Sato, T. *et al.* Long-term expansion of epithelial organoids from human colon, adenoma, adenocarcinoma, and Barrett's epithelium. *Gastroenterology* **141**, 1762–72 (2011).

42.   Dobin, A. *et al.* STAR: ultrafast universal RNA-seq aligner. *Bioinformatics* **29**, 15–21 (2013).

43.   Li, B. & Dewey, C. N. RSEM: accurate transcript quantification from RNA-Seq data with or without a reference genome. *BMC Bioinformatics* **12**, 323 (2011).

44.   Love, M. I., Huber, W. & Anders, S. Moderated estimation of fold change and dispersion for RNA-seq data with DESeq2. *Genome Biol.* **15**, 550 (2014).

45.   Luo, W., Friedman, M. S., Shedden, K., Hankenson, K. D. & Woolf, P. J. GAGE: generally applicable gene set enrichment for pathway analysis. *BMC Bioinformatics* **10**, 161 (2009).

46.   Luo, W. & Brouwer, C. Pathview: an R/Bioconductor package for pathway-based data integration and visualization. *Bioinformatics* **29**, 1830–1 (2013).

47.   Thompson, L. R. *et al.* A communal catalogue reveals Earth's multiscale microbial

diversity. *Nature* **551**, 457–463 (2017).

48.   Marotz, C. *et al.* DNA extraction for streamlined metagenomics of diverse

environmental samples. *Biotechniques* **62**, 290–293 (2017).

49.   Amir, A. *et al.* Deblur Rapidly Resolves Single-Nucleotide Community Sequence

Patterns. *mSystems* **2**, (2017).

50.   Kuczynski, J. *et al.* Using QIIME to analyze 16S rRNA gene sequences from

microbial communities. *Curr. Protoc. Bioinforma.* **Chapter 10**, Unit 10.7. (2011).

51.   Lee, W. N. *et al.* In vivo measurement of fatty acids and cholesterol synthesis using

D2O and mass isotopomer analysis. *Am. J. Physiol. Metab.* **266**, E699–E708 (1994).

52.   Wallace, M. *et al.* Enzyme promiscuity drives branched-chain fatty acid synthesis in

adipose tissues. *Nat. Chem. Biol.* **14**, 1021–1031 (2018).

53.   Kireeva, M. L., MO, F. E., Yang, G. P. & Lau, L. F. Cyr61, a product of a growth

factor-inducible immediate-early gene, promotes cell proliferation, migration, and

adhesion. *Mol. Cell. Biol.* **16**, 1326–1334 (1996).

54.   Mandal, S. *et al.* Analysis of composition of microbiomes: a novel method for

studying microbial composition. *Microb. Ecol. Health Dis.* **26**, 27663 (2015).

Figure Legends

Figure 1. High-fructose diet induces hepatosteatosis and tumorigenesis. (**a**) *MUP-uPA*

mice were fed CSD or HFrD. After 5 months, formalin-fixed, paraffin-embedded (FFPE) and

frozen sections of non-tumor liver tissue were stained with H&E or Oil Red O (ORO) to

reveal general histology and lipid droplets (n = 6 per group). Collagen deposition was

visualized by Sirius Red staining of frozen sections. Scale bars, 100 μm. (**b**) Liver samples

were also analyzed for total triglyceride (TG) content (n = 6), which is presented as fold-

change relative to CSD-fed mice. (**c**) Liver morphology of CSD- and HFrD-fed *MUP-uPA*

mice. (**d**) HCC development in CSD- or HFrD-fed *MUP-uPA* mice (n = 9). (**e**) HCC in DEN-

challenged BL6 mice fed CSD or HFrD (n = 9-11).Panels **b,d** and **e** show mean ± SEM asdetermined by two-sided Student's *t* test, *P < 0.05, ***P < 0.001.

Figure 2. HFrD induces inflammation, lipogenic gene expression and *de novo* lipogenesis. (**a** and **b**) Expression of lipogenic (**a**) and inflammatory (**b**) genes in *MUP-uPA* and DEN-challenged BL6 mice fed either CSD or HFrD for 5 months (n = 7-10). (**c**) Immunoblot (IB) analysis of ACC1 and FAS in livers of above *MUP-uPA* mice. (**d**) Measurement of newly synthesized fatty acids in livers of *MUP-uPA* mice using deuterated water (D_2O) as a tracer (n = 7). Panels **a,b** and **d** show mean ± SEM determined by two sided Student's *t* test,*P < 0.05, **P < 0.01, ***P < 0.001.

Figure 3. Fructose causes barrier deterioration, decreased tight junction protein expression and ER stress. (**a**) Fecal albumin concentrations in *MUP-uPA* mice kept on CSD or HFrD or HFrD ± Abx (n = 6-7 per group). (**b** to **c**) Tight junction mRNAs in colonic (**b**) and jejunal (**c**) mucosa of CSD- or HFrD-fed (5 months) *MUP-uPA* mice (n = 7-9 per group). (**d**) Tight junction mRNAs in BL6 enteroids incubated with glucose (Glu) or fructose (Fru) (n = 4 per group). (**e**) Expression of inflammatory and ER stress markers in colonic mucosa of above mice (n=9) and a phspho-eIF2α blot of mucosal lysates. Panels **a-e** show mean ± SEM determined by two sided Student's *t* test, *P < 0.05, **P < 0.01, ***P < 0.001.

Figure 4. HFrD-induced upregulation of liver TLR and cytokine signaling and role of myeloid MyD88. (**a**) Heatmaps depicting differential expression of genes related to inflammation wound healing and innate immunity in livers of CSD- or HFrD-fed (5 months) *MUP-uPA mice*. (**b**) Expression of inflammatory chemokines and cytokines mRNAs in above mice. (**c**) IB analysis of TLRs, MyD88, phosphorylated and total STAT3 and NLRP3 in livers of 6-month-old *MUP-uPA* mice fed CSD or HFrD or HFrD ± Abx for 5 months (n = 7-9). (**d** and **e**) Expression of lipogenic and inflammatory genes (**d**) and IB analysis of ACC1 and FAS (**e**) in livers of *Myd88$^{\Delta mye}$* and WT mice fed HFrD for 5 months (n = 8). (**f**)

Liver triglyceride content in above mice (n = 8; mg/g tissue). Panels **b**,**d** and **f** show mean ±

SEM determined by two-sided Student's *t* test, **P* < 0.05, ***P* < 0.01.

Figure 5. Activated gp130 suppresses fructose-induced hepatic tumorigenesis, DNL

and lipogenic and inflammatory gene expression. (**a**) HCC burden in CSD- or HFrD-fed

MUP-uPA/gp130^{Act} (*MUP-uPA*/Tg) mice and HFrD-fed *MUP-uPA* mice (*n* = 9 per group). (**b**)

Liver lipogenic and inflammatory mRNAs in *MUP-uPA/gp130^{Act}* mice fed CSD or HFrD and

MUP-uPA mice fed HFrD (*n* = 9 per group). (**c**) Liver fatty acid synthesis in *MUP-uPA* and

MUP-uPA/gp130^{Act} mice administered D$_2$O as a tracer (n=7 per group). (**d** to **f**) Control BL6

mice and mice overexpressing the antimicrobial protein Reg3β in intestinal epithelial cells

were fed CSD or HFrD for 3 months. (**d**) Frozen liver sections were ORO stained to reveal

lipid droplets (*n* = 3 per group). Scale bars, 100 µm. (**e**) Relative mRNA amounts of liver

lipogenic and inflammatory genes and (**f**) body weight in above mice (*n* = 4-5). Panels **a-c**

and **e-f** show mean ± SEM determined by two-sided Student's *t* test, **P* < 0.05.

Figure 6. TNF stimulates lipid droplet accumulation and lipogenic enzyme induction

in human hepatocytes and schematic summary of the mechanism by which fructose

intake stimulates hepatic DNL and steatosis. (**a,b**) Human hepatocytes isolated from two

healthy donors were placed in sugar-free medium or in the presence of 5 mM fructose or

glucose. LPS or TNF were added as indicated and 2 days later the cells were evaluated by

ORO staining for lipid accumulation and qRT-PCR for DNL-related mRNAs (n=3;

mean ± SEM by two- sided Student's t test). (**c**) Schematic summary. In IEC dietary fructose

is converted to F1P by KHK. F1P inhibits protein N-glycosylation triggering ER stress and

intestinal inflammation to downregulate tight junction proteins (TJP) and trigger barrier

deterioration and endotoxemia. Endotoxin (LPS) reaches the liver via the portal vein and

engages TLR4 on macrophages to activate NF-κB via the adaptor protein MyD88 and

induce TNF expression and secretion. TNF engages TNFR1 on hepatocytes to induce

caspase-2 (Casp2) mRNA whose translation is stimulated by ER stress-activated IRE1.

Casp2 activates SREBP1 to induce ACC1 and FAS, thereby priming the liver to convert

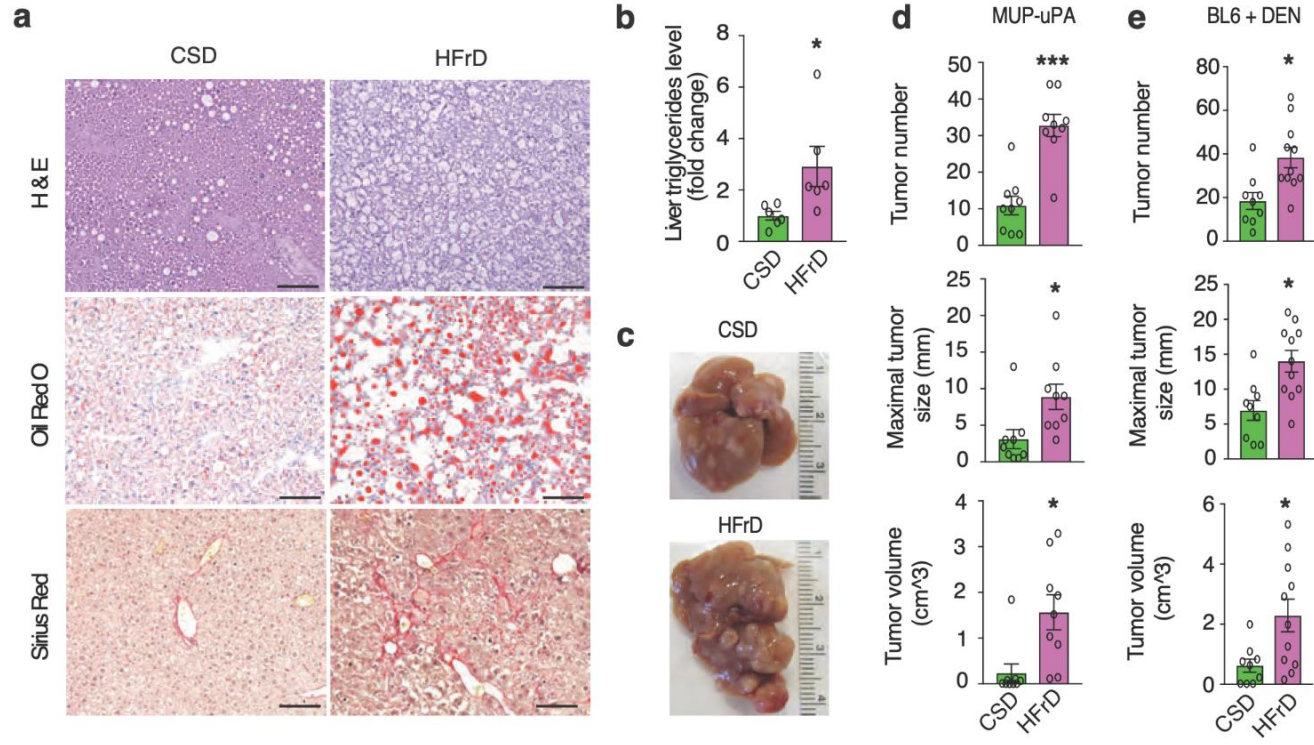KHK-generated F1P to FA (C:16/C:18), giving rise to hepatosteatosis.
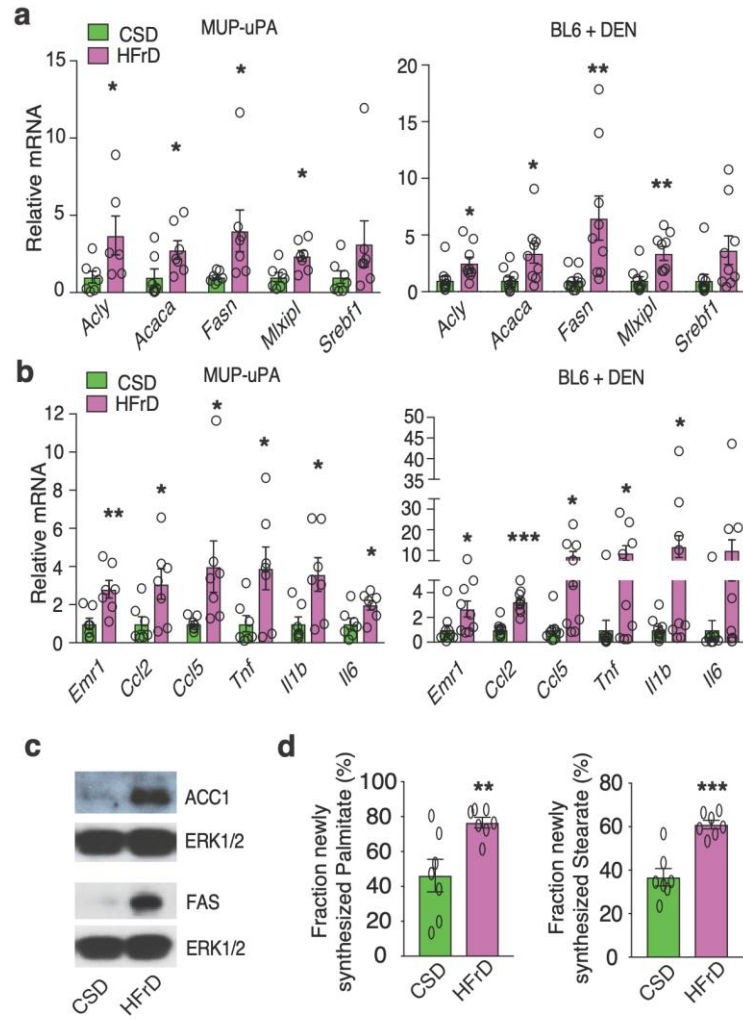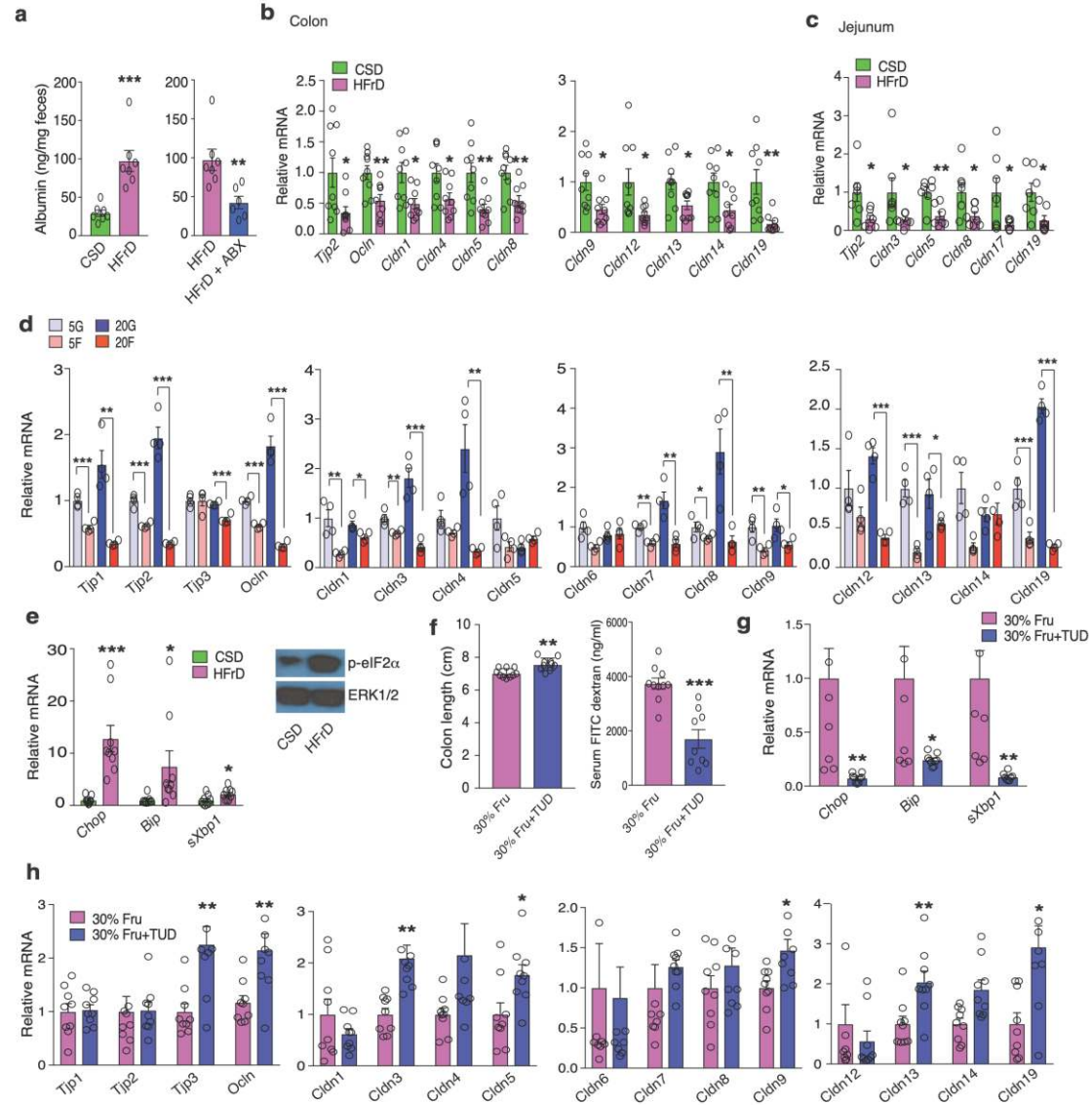
Figure 1

Figure 2
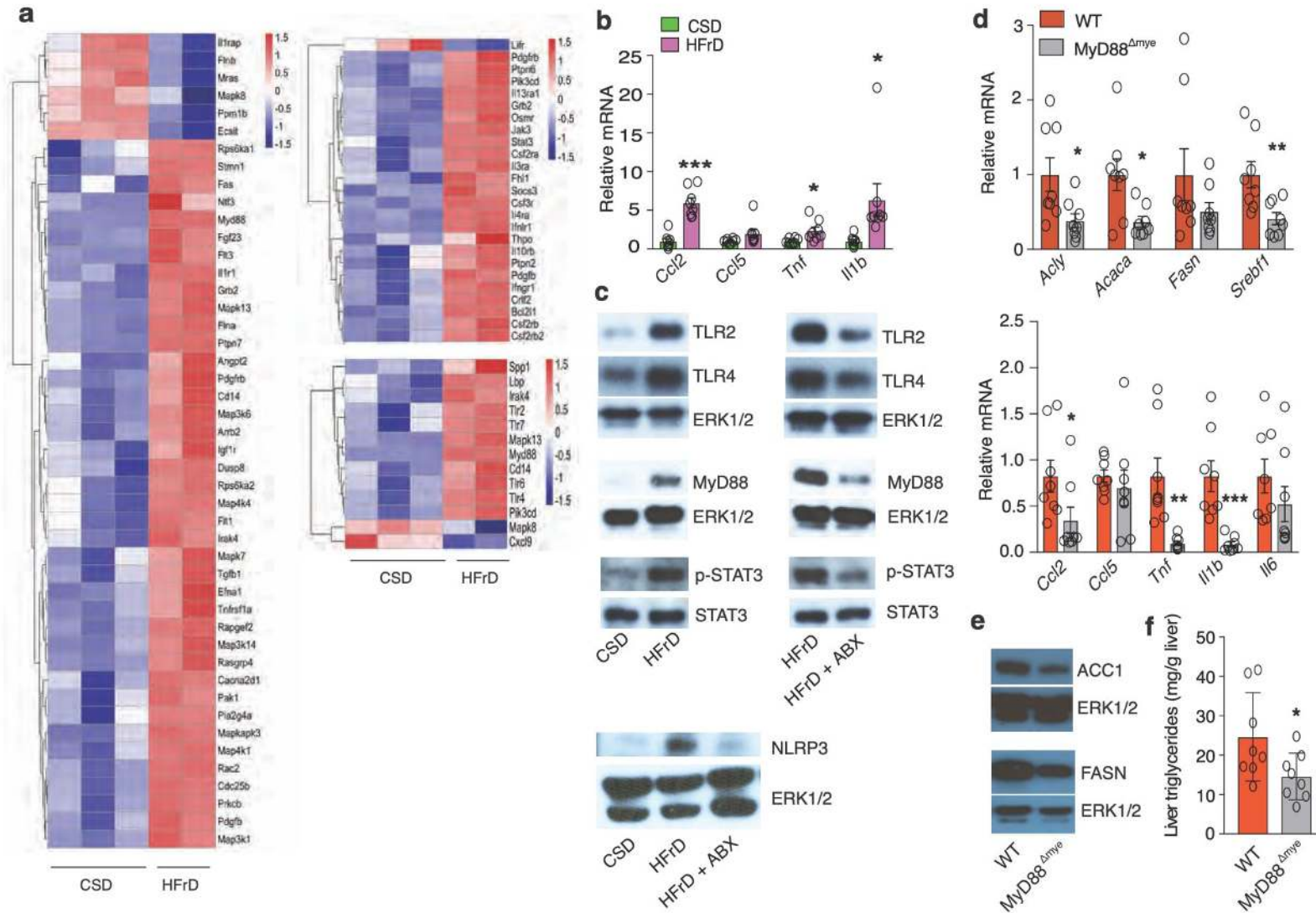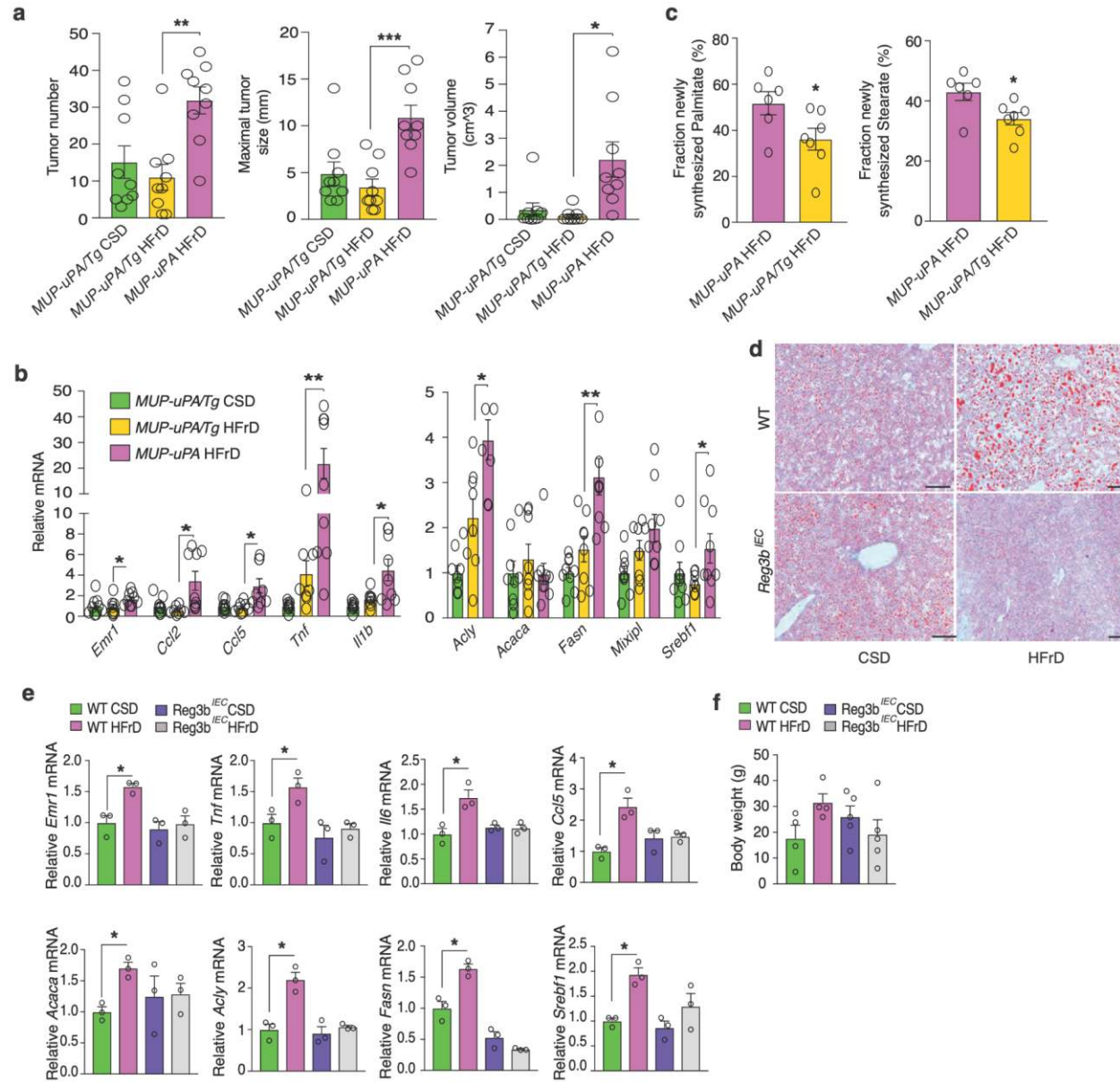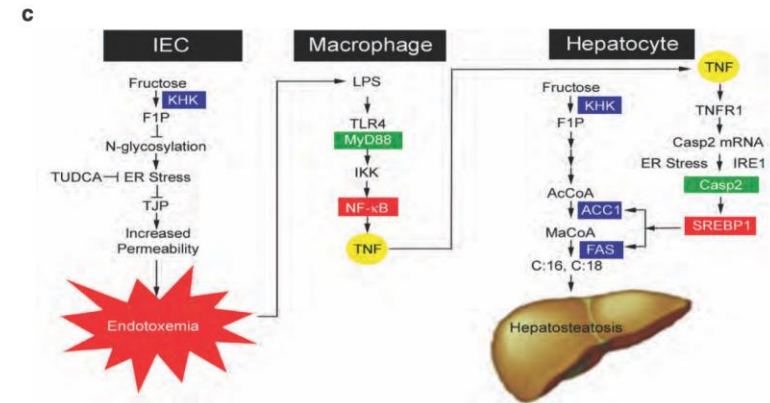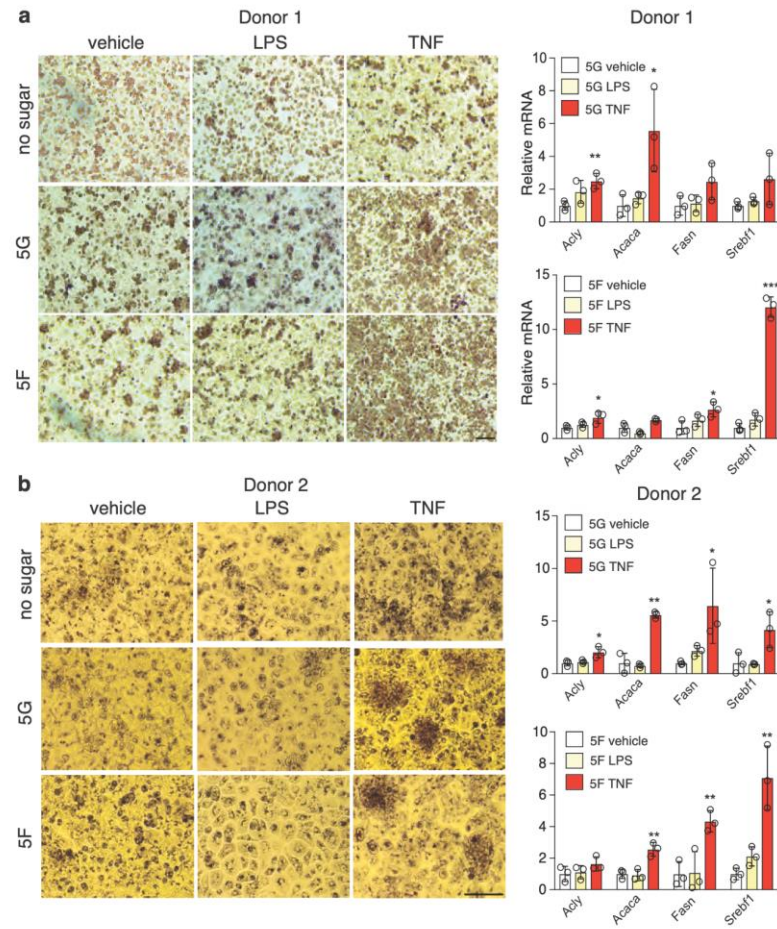
Figure 3

Figure 4

Figure 5

Figure 6

Extended Data

Extended Data Figure 1. HFrD stimulates HCC development without affecting body weight or white adipose tissue. (a) Food consumption by *MUP- uPA* and BL6 mice given CSD or HFrD (n = 9-12). **(b)** Formalin-fixed, paraffin-embedded (FFPE) and frozen liver tissue sections of DEN- challenged BL6 mice were stained with H&E or ORO (n = 6). Scale bars, 100 µm. **(c)** Total triglyceride content in livers of DEN-challenged BL6 mice (n = 6) is presented as fold-change relative to CSD-fed mice. **(d** and **e)** Body and WAT weight of *MUP-uPA* (n = 9) **(d)** and DEN- challenged BL6 (n = 9-12 per group) **(e)** mice given CSD or HFrD were measured at the indicated time points. **(f)** Colon length in indicated mice (n = 9-12 per group). **(g** and **h)** *MUP-uPA* mice (n = 15 per group) **(g)** or DEN-challenged BL6 mice (n = 13-16 per group) **(h)** fed HFrD (▲) or CSD (■) for 5 months were subjected to glucose tolerance tests (GTT). **(i** and **j)** CSD- or HFrD- fed *MUP-uPA* mice (n = 4 per group) **(i)** or DEN-challenged BL6 mice (n = 6 per group) **(j)** were placed in metabolic cages for two-and-a-half 24-hour cycles composed of two 12-hour light periods and three dark periods. VO_2, VCO_2, heat production and body weights were measured. **(k)** Non-fasting serum insulin was measured by ELISA in indicated mice (n=7-8). **(l)** Liver tumor histology in *MUP-uPA* and DEN-challenged BL6 mice given either CSD, HFrD, or HFrD + Abx cocktail (n = 7-12). FFPE tumor sections were stained with hematoxylin and eosin (H&E). Scale bars, 100 µm. Unpaired two-sided Student's t test was used in panels c to f and i to k, whereas Mann-Whitney test was used in panels g and h. Mean ± SEM, *$P < 0.05$, **$P < 0.01$, ***$P < 0.001$.

Extended Data Figure 2. Regulation of fructose-stimulated DNL and lipogenic enzymes. **(a)** Cytosolic acetyl-CoA concentrations in 6-month-old CSD and HFrD fed *MUP- uPA* mice (n = 7-9). **(b)** Expression of genes encoding FA-oxidizing enzymes in CSD- or HFrD- fed (5 months) *MUP-uPA* and DEN-challenged BL6 mice (n = 7-10). **(c)** A metabolic chart comparing pathways through which glucose and fructose are converted to acetyl-CoA in the cytoplasm. GK-glucokinase; KHK-ketohexokinase; GI-glucose isomerase; PFK-phosphofructokinase. Cytoplasmic acetyl-CoA is converted to malonyl-CoA by acetyl-CoA carboxylase (ACC) and malonyl-CoA serves as the building block for synthesis of C16:0 (palmitate) and C18:0

(stearate) by fatty acid synthase (FAS). Expression of ACC1 and FAS is strongly upregulated by prolonged HFrD feeding. (**c** and **d**) Measurement of newly synthesized FA in livers (**d**) and jejunum (**e**) of *MUP-uPA* mice using D_2O as a tracer after a short-term feeding period (48 hours; n = 7). (**f**) Amounts of F1P in liver and jejunum expressed in arbitrary units (48 hours feeding; n = 7). (**g** and **h**) Expression of inflammatory and lipogenic genes and ACC1 protein in livers (**g**) and fecal albumin and serum FITC-dextran concentrations (**h**) in CSD- or HFrD-fed (48 hours) mice (n = 7). Unpaired two-sided Student's t test was used in panels a, b and d-h. Mean ± SEM, *$P < 0.05$, **$P < 0.01$.

Extended Data Figure 3. HFrD feeding causes downregulation of TJP, ER stress, colonic inflammation and barrier deterioration. (**a** and **b**) Expression of TJP genes in colon (**a**) and jejunum (**b**) of *MUP- uPA* mice fed HFrD with or without concomitant Abx treatment (n = 6-9). (**c**) IB analysis of indicated TJP in colon tissue of above mice (n = 7-9). (**d**) Expression of *Il22* mRNA and IL-22 regulated genes in colon tissue of CSD-, HFrD-, or HFrD + Abx-fed *MUP-uPA* mice (n = 7-9). (**e** and **f**) BL6 mice were given 30% fructose in drinking water or regular water and fed NCD for 5 (**e**) or 3 (**f**) months and mRNA amounts of TJP genes in colon and jejunum (**e**), colon length and FITC-dextran serum levels were measured (**f**). (**g** to **h**) BL6 mice were given 30% fructose or 30% sucrose in drinking water and fed NCD for 3 months and colon length and FITC-dextran serum levels (**g**), colon TJP mRNAs (**h**) and ER stress marker mRNAs (**i**) were measured. (**j**) *Chop* and *sXbp1* mRNA amounts in fructose and glucose treated organoids (n=3). (**j-m**) Expression of indicated mRNAs in BL6 enteroids maintained in media containing the indicated glucose and/or fructose concentrations (mM) (n = 3-4) and treated with KHK inhibitor (**k** and **l**), TUDCA (**m**) or vehicle. Unpaired two-sided Student's t test was used in all panels, other than c, to determine Mean ± SEM, *$P < 0.05$, **$P < 0.01$, ***$P < 0.001$.

Extended Data Figure 4. Fructose-induced alterations in the liver transcriptome. (a) KEGG pathway map of innate immune signaling with HFrD-induced genes indicated in red. (**b**) Heatmap depicting the entire transcriptome of non-tumor liver tissue from DEN-treated BL6 mice kept on CSD or HFrD for 5 months and analyzed immediately thereafter. **(c)** Heatmap depicting the entire

transcriptome of tumor-bearing liver tissue from DEN-treated BL6 mice kept on CSD or HFrD until 9 months old. (**d**) Heatmap depicting expression of HCC-related genes in non-tumor and tumor liver tissues from mice described in (**b**). The color code represents relative mRNA abundance where red shows overexpression and blue shows under expression. (**e**) Most significant Gene Ontology enrichment terms for Biological Pathways for the genes shown in heatmap (**b**) comparing DEN-treated BL6 mice fed a CSD or HFrD at 6 months of age. The bigger the dot, the more genes fall in the respective category. The color code represents the adjusted *P*-value (all are significant and below a cut-off level of 0.01) determined using Benjamini-Hochberg FDR adjustment.

Extended Data Figure 5. Fructose-induced endotoxemia, hepatosteatosis, HCC, liver fibrosis, glucose intolerance and colonic inflammation are inhibited by antibiotics. (a) CSD and HFrD-fed *MUP-uPA* and DEN- challenged BL6 mice were treated or not with a broad-spectrum Abx cocktail for 5 months, after which serum endotoxin concentrations were measured (n = 7-9). (**b**) HCC burden in *MUP-uPA* and DEN-challenged BL6 mice given HFrD alone or HFrD plus Abx cocktail (n=7-11). (**c**) Hepatosteatosis in *MUP-uPA* and DEN-challenged BL6 mice given HFrD ± Abx for 5 months determined by ORO staining of liver sections. Scale bars, 100 µm. (**d**) Liver triglyceride content in above mice (n = 6). (**e - g**) Expression of lipogenic (**e**) and inflammatory (**f**) genes and IB analysis of liver ACC1 and FAS (**g**). (**h, i**) Liver F1P abundance (*MUP-uPA*; n = 7) (**h**) and cytosolic acetyl-CoA (n = 7-8; the HFrD bar is same as in Extended Data Figure 2**a**). (**j, k**) glucose tolerance (**j**) and non-fasting serum insulin (n=7) (**k**). (**l**) Total body and white adipose tissue weights in indicated mice (n=7-12) (**m**) Liver fibrosis in HFrD-fed *MUP-uPA* mice was examined by Sirius Red staining (n = 7). (**n**) Colon length in indicated mouse strains (n = 7-9; the HFrD bars are same as in Extended Data Figure 1**f**). Scale bars, 100 µm. Unpaired two-sided Student's t test was used in panels a, b, d-f, h, I, k, l and n to determine mean ± SEM, whereas panel j was analyzed using a Mann-Whitney test. *$P < 0.05$, **$P < 0.01$, ***$P < 0.001$.

Extended Data Figure 6. Antibiotics attenuate fructose-induced hepatosteatosis, barrier deterioration and other alterations in BL6 mice. (a to **g**) BL6 mice were fed CSD or HFrD

± Abx. (**a**) After five months, liver tissue sections were stained with ORO (n = 9). Scale bars, 100 μm. (**b** and **c**) Inflammatory and DNL-related mRNAs in liver were determined by Q-RT-PCR (n = 9). (**d** and **e**) Inflammatory and lipogenic proteins in liver lysates were analyzed by IB analysis (n = 9). (**f** and **g**) Q-RT-PCR analysis of indicated TJP genes in jejunum (**f**) and colon (**g**) (n = 9). Two-sided Student's t test was used to determine mean ± SEM, *$P < 0.05$, **$P < 0.01$, ***$P < 0.001$.

Extended Data Figure 7. Fructose drink enhances hepatosteatosis, expression of liver mRNAs encoding inflammatory cytokines and DNL-related enzymes and barrier deterioration. (**a-c**) BL6 mice were placed on 30% fructose in drinking water or regular water and NCD for 5 months (n = 8). (**a**) Liver sections were ORO stained. (**b**) mRNA amounts of liver inflammatory and DNL-related genes were PCR analyzed. (**c**) Total body, liver and white adipose tissue weights were measured. (**d** - **h**) BL6 mice placed on 30% fructose drink or regular water and HFD for 3 months. Body, liver and WAT weight and liver/body weight ratio were determined (n = 8). (**d**) Liver sections were analyzed by ORO staining. (**e**) Liver mRNAs encoding cytokines and DNL-related proteins were measured using Q-RT-PCR (n = 7) (**f**). Expression of TJP mRNAs in colon (n = 7) (**g**) and FITC-dextran in serum (n = 6) (**h**) were also measured. Scale bars, 100 μm. Two-sided Student's t test was used to determine mean ± SEM,*$P < 0.05$, **$P < 0.01$, ***$P < 0.001$.

Extended Data Figure 8. Fructose-induced upregulation of YAP target genes and attenuation of TJP mRNA downregulation, barrier deterioration, hepatosteatosis and induction of DNL-related proteins in *MUP-uPA/gp130^{Act}* and CCN1-treated mice. (**a,b**) Expression of indicated mRNAs in BL6 enteroids maintained in media containing the indicated glucose and fructose concentrations (mM) (n = 3) (**a**) and in colonic mucosa of *MUP-uPA* mice (n = 7-8) (**b**) was measured by Q-RT-PCR. (**c**) Enteroids from *MUP-uPA* and *MUP-uPA/gp130^{Act}* mice (n = 4) were incubated with 20 mM fructose. Expression of indicated mRNAs was measured by Q-RT-PCR. (**d** and **e**) Expression of anti-microbial (**d**) and TJP (**e**) mRNAs in colon tissues of *MUP-uPA/gp130^{Act}* (*MUP-uPA*/Tg) mice fed CSD or HFrD compared to *MUP-uPA* mice fed HFrD for five months (n = 9). Asterisks indicate significant

changes between *MUP-uPA* and *MUP-uPA*/Tg mice fed HFrD. (**f**) IB analysis of claudin-1 in colons of *MUP-uPA/gp130^{Act}* and *MUP-uPA* mice kept on CSD or HFrD as indicated. (**g**) FITC-dextran serum concentrations in indicated mice (n = 6). (**h**) Serum endotoxin concentrations in indicated mice measured by ELISA. (**i**) F1P abundance in liver and jejunum of indicated mice (arbitrary units; n = 7). (**j** to **p**) 6-week-old *MUP-uPA* mice were fed HFrD for 3 months and i.p. injected 2 μg CCN1 or vehicle (PBS) every other day for the last 4 weeks of HFrD feeding. Length (**j**) and TJP mRNA expression (**k**) were determined on excised colons (n = 7). Fecal albumin was measured by ELISA (n = 8) (**l**). ORO staining and triglyceride concentrations (n = 7) (**m**), inflammatory and lipogenic gene expression (n = 7) (**n**) and FAS protein amounts (n = 7) (**o**) were measured in liver tissue. (**p**) Body weight was measured at the end of the CCN1 treatment course (n = 7). (**q**) Endotoxin levels in serum of indicated mice (n=3) Scale bars, 100 μm. Two-sided Student's t test was used to determine mean ± SEM, *P < 0.05, **P < 0.01, ***P < 0.001.

Extended Data Figure 9. Low-dose LPS treatment stimulates hepatosteatosis and increases lipogenic and inflammatory gene expression and effect of fructose on microbiome diversity. (**a** to **c**) Six-week-old *MUP- uPA* mice were fed CSD and received daily i.p. injections of LPS (0.25 mg/kg) or vehicle (PBS) or were fed HFrD for 3 months. (**a**) ORO staining of liver sections (n = 8). (**b**) Liver triglyceride concentrations in above mice (n = 7). (**c**) Q-RT-PCR analysis of lipogenic and inflammatory mRNAs (n = 8). (**d** to **f**) Six-week-old *MUP-uPA/Tg* mice were fed HFrD and received daily i.p. injections of LPS or PBS and compared to *MUP-uPA* mice that were fed HFrD only.(**d**) ORO staining of liver sections (n = 8; scale bars, 100 μm). (**e**) Liver triglyceride concentrations (n = 7). (**f**) Relative mRNA amounts of lipogenic and inflammatory genes (n = 8). (**g** and **i**) Relative abundance of significantly differing taxa. Significance was determined by ANCOM. Box-plots of observed operational taxonomic units (OTUs) α-diversity indices comparing stool samples of *MUP-uPA* (**g**) and *MUP-uPA/*Tg (**i**) mice treated as indicated. (**h** and **j**) Principal coordinate analysis of microbiome data using unweighted UniFrac distances; difference between CSD and HFrD was

significant in both *MUP-uPA* (**h**) (pseudo-*F* statistic = 2.88, *P* < 0.001, n = 10 and 24) and

*MUP-uPA/*Tg (**j**) (pseudo-*F* statistic = 9.19, *P* < 0.001, n = 11 and 12) mice as determined by

PERMANOVA. Two-sided Student's t test was used in panels b,c,e and f to determine mean

± SEM, **P* < 0.05, ***P* < 0.01, ****P* < 0.001.

Extended Data Table 1. Primer sequences

Gene name	Forward (5' - 3')	Reverse (5' - 3')
Acly	CTGTGCCACCATGTTCTCCTC	AGGCCTGGTTCTTGGCTACTG
Acaca	TTCCACGTAGGAGGAGCTTCC	CCTCCGGTGCCTTCTCATTAC
Fasn	AGAAGAGCCATGGAGGAGGTG	ATGTCCACACCACCAATGAGG
Mlxipl	CGGATACGGACTTGGAGGATC	GAAGTGTCCGCTGTGGATGAC
Srebf1	GATCAAAGAGGAGCCAGTGC	TAGATGGTGGCTGCTGAGTG
Emr1	GACTGACAACCAGACGGCTTG	TCACTGCCTCCACTAGCATCC
Tnf	GCACAGAAAGCA TGACCCG	GCCCCCCA TCTTTTGGG
Ccl2	GCCAGCTCTCTCTTCCTCCA	CCCAGAAGCA TGACAGGGAC
Ccl5	AATCCCCTACTCCCACTCGG	TTCTTGGGTTTGCTGTGCAG
Il1b	CAACCAACAAGTGATATTCTCCAT G	GATCCACACTCTCCAGCTGCA
Il6	GAGGATACCACTCCCAACAGACC	AAGTGCATCATCGTTGTTCATACA
Cldn1	ATCACCTTCGGGAGCTCAGGT	TGATGGGGGTCAAGGGGTCAT
Cldn3	CTGGTCGGCCAACACCATCAT	ATGGTTTGCCTGTCTCTGCCC
Cldn4	GCAGAGCACAGGTCAGATGCA	AGGGCAGGTCCTGGAGAATGT
Cldn5	TGGACCACAACATCGTGACGG	TGCCTCCCGCCCTTAGACATA
Cldn6	CCCTTGGTGGCTGATGCTCAA	AGGTGGAGCTTGGACTCAGGT
Cldn7	AACATCATCACAGCCCAGGCC	ATGTTTGGAGGTGGAGTGGCC
Cldn8	GTGCTTGGTGGTGTTGGCATG	CGTTGAGTGGTGCGATGGGAT
Cldn9	AAGTGGTATGGGAGGGGCTGT	CGCAGGTGGAAGCTTCTGGAA
Cldn12	TGTGTGCAGATGTGCTCCTGT	GCAGGAGGGCTTGAGCTGTAT
Cldn13	GGCTCTTGGAATCCTGCATCT	TGGCATCTGGGTCTGTCTCAT
Cldn14	CTAACCAGAGGGCATGTGTGC	AGTCCCATCCACCTTGATGCT
Cldn19	GGAATTCTTCAACCCCAGCAC	ATAGGGCTGTGGGATGCTGTT
Ocln	TCCGGATCCTGTCTATGCTCA	ATAGCCACCTCCGTAGCCAAA
Tjp1	GAAACTCTGCTGAGCCCCCTA	GTTTTAGGGTCACCCGACGAG
Tjp2	CGAAGCAGTCTGGGTCTCTGA	CCGGCTCCTCTAGCTCATTGT
Tjp3	ATGGTATGCCATTTCGGAACC	CCGGGTACAACGTGTCCACTA
Ctgf	CAGAGTGGAGCGCCTGTTCTA	AGGTGTCCGGATGCACTTTTT
Ccne	GTCTGCAAGATGCCTTGGATG	CAACCTACAACACCCGAGCAG
Reg3b	ATGGCTCCTACTGCTATGCC	GTGTCCTCCAGGCCTCTTT
Reg3g	ATGGCTCCTATTGCTATGCC	GATGTCCTGAGGGCCTCTT
Lcn2	ACATTTGTTCCAAGCTCCAGGGC	CATGGCGAACTGGTTGTAGTCCG
Il22	GGCCAGCCTTGCAGATAACA	GCTGATGTGACAGGAGCTGA
S100a9	GGTGGAAGCACAGTTGGCA	GTGTCCAGGTCCTCCATGATG
18s	AGCCCCTGCCCTTTGTACACA	CGATCCGAGGGCCTCACTA